From voxels to scalpels

Validation of a dissection and imaging protocol for measuring musculoskeletal model parameters

I.T. van Kan

TU Delft

From voxels to scalpels

Validation of a dissection and imaging protocol for measuring musculoskeletal model parameters

by

Iris Thérèse van Kan

to obtain the degree of Master of Science

at the Delft University of Technology,

to be defended publicly on Thursday September 18, 2025 at 2:00 PM.

Student number:	4840038	
Project duration:	February 1, 2025 – September 18, 2025	
Thesis committee:	Dr. ir. E. van der Kruk,	TU Delft, daily supervisor and chair
	Dr. ir. B. Bolsterlee,	TU Delft, supervisor
	Dr. H. P. Theeuwes,	Erasmus Medical Centre, supervisor
	Prof. Dr. F. C. T. van der Helm,	TU Delft, external committee member

An electronic version of this thesis is available at `http://repository.tudelft.nl/`.

TU Delft

Contents

From voxels to scalpels: Validation of a dissection and imaging protocol for measuring musculoskeletal model parameters

Iris Thérèse (I.T) van Kan

Abstract

Musculoskeletal models lack in vivo variability because their muscle parameters are scaled from limited dissection studies. Magnetic resonance imaging (MRI) could provide in vivo data, but its validation against dissection is challenged: the lengthy duration of dissection requires fixation to prevent tissue decay, yet fixation itself possibly introduces unquantified artifacts. The aim was two-fold; (1) to understand the effects of fixation on MRI-derived muscle volume, and (2) to evaluate the feasibility of handheld 3D scanning, for measurement of muscle fibers, origins, and insertions, to accelerate dissection studies, thereby potentially eliminating the need for fixation. MRI and handheld 3D scanning were verified against measurements of muscle weight, volume, and 3D digitizer measurements. We performed MRI on one fresh-frozen specimen, before and after AnubiFIX™ fixation. Followed by a dissection of 20 thigh muscles, with 3D handheld scanning to capture muscle surfaces, while muscle fibers, origins and insertions were measured with a 3D digitizer. Fixation caused a substantial 31.5% (SD 23.3%) muscle volume increase; separately, a methodological bias of MRI volumes systematically exceeding dissected volumes (+48.1 cm^3), likely due to tissue dehydration during dissection. While handheld scanning reduced measurement time by 15-20 hours, it provided only partial visibility of muscle fibers (50%), origins (40%) and insertions (35%). By highlighting the volumetric effects of fixation and dehydration in muscles, and assessing handheld 3D scanning during dissection, this work provides a foundational framework for more meaningful comparisons between MRI and dissection for musculoskeletal models.

Keywords: musculoskeletal models, magnetic resonance imaging (MRI), muscle architecture, handheld 3D scanning, dissection validation, tissue fixation

1. Introduction

Understanding how muscles generate force and contribute to joint loading is useful for studying human movement, injury, and rehabilitation. These quantities cannot be measured directly in humans, which has led to the development of computational musculoskeletal models. These models allow researchers to study movement mechanics, test hypotheses about muscle function, and simulate surgical interventions.

Musculoskeletal models use rigid bodies, joints, and muscles models to represent the human body. Hill-type models are most widely adopted to simulate muscle force due to their balance between computational efficiency and physiological accuracy. These phenomenological models represent muscle as a contractile element with force-generating properties that depend on muscle length, contraction velocity, and activation level. Musculoskeletal simulation platforms like OpenSim (1), scale muscle architecture parameters to match the characteristics of an individual. However, because the muscle architecture parameters used in these models are derived from a limited number of dissection studies, these scaled parameters do not represent variable, in vivo anatomy (2; 3). Force predictions from musculoskeletal models are especially sensitive to muscle architecture parameters, in particular optimal fiber length, physiological cross-sectional area, and tendon slack length (4). Therefore, accurate measurement of these muscle properties is essential for reliable model predictions.

Muscle model parameters have been estimated using a variety of techniques, with dissection remaining the gold standard (5). In traditional dissection protocols, muscles were fixed to preserve tissue integrity, then carefully isolated by removing surrounding connective tissue to expose individual fiber bundles. Muscle fiber lengths (L_f) and pennation angles (θ_f) are measured directly from these bundles using calipers or rulers to capture the anatomical arrangement of the muscle. Historically, these studies have provided the foundational muscle data for musculoskeletal models. Now, these studies serve as a reference for validating imaging derived parameters. Emerging techniques like Diffusion Tensor Imaging (DTI) are non-invasive, more accessible techniques and offer the potential to visualize and quantify muscle architecture parameters like L_f and θ_f in vivo (5; 6). A key distinction is that while these models parameterize the 'muscle fiber', experimental techniques like DTI and dissection measure the the muscle fascicle. Although muscle fibers may not span the entire length of a fascicle, they function as a single contractile unit. Therefore, as this paper focuses on Hill-type model parameters, 'fiber' is used throughout when referring to measured fascicle properties.

Hill-type muscle model inputs that require muscle architecture are: optimal fiber length ($L_{f_{opt}} = L_f \cdot \frac{L_s}{L_{s_{opt}}}$), where L_s is the measured sarcomere length and $L_{s_{opt}}$ the optimal sarcomere length; the physiological cross-sectional area ($PCSA = V_m/L_{opt}$), where V_m is muscle volume; θ_f represents the angle between muscle fibers and the line of action, which determines the projection of fiber force onto the tendon; and muscle moment arms (r) representing the perpendicular distance from the joint center of rotation (JCR) to the muscle's line of action (LoA). The LoA requires the attachments sites of the muscle (origin, insertion) as its endpoints. MRI might provide the data needed to estimate L_f and θ_f from DTI-MRI, and V_m, JCR and LoA from anatomical MRI. However, confirming that these MRI-derived muscle architecture parameters accurately reflect true anatomical values is essential, which makes their validation against dissection a critical step.

Dissection measurement methods

In more recent dissection studies, the most detailed 3D reconstructions of the architecture of human muscles have been made through micro-dissection and digitization, using, for example, the MicroScribe™ system (7; 8). While accurate, this point-by-point approach is laborious and requires muscles to be excised, eliminating their natural positioning and wrapping patterns. Some dissection studies supplement digital measurements with 2D photography for documentation purposes, but these images serve primarily as visual records rather than quantitative surface or volumetric data sources (9). In contrast to 2D photo and point-based approaches, surface scanning methods offer rapid 3D data capture. In particular, handheld 3D scanning technology has revolutionized surface digitization in fields ranging from anthropology to industrial design (10; 11). These devices capture detailed surface geometry in minutes rather than hours. Several studies already demonstrated this advantage and their accuracy in biological specimens, particularly for documenting bone geometry and skeletal remains (12). While handheld scanners have proven effective for hard tissue digitization, their application on soft tissue, in for example anatomical dissection contexts remains unexplored (13).

To evaluate the potential of handheld 3D scanning for measuring muscle model parameters, Table 1 compares its capabilities with established techniques like MRI and dissection. Sarcomere length (L_s) was excluded from this study, as its measurement requires laser diffraction, a method that analyzes the light pattern from a laser passing through a muscle fiber. The Line of Action (LoA) and Joint Center of Rotation (JCR) were also excluded, as their dissection-derived values are not meaningful in an ex vivo, unloaded state. Therefore, the primary potential of handheld 3D scanning lies in measuring fiber length (L_F), pennation angle (θ_f), and the locations of muscle origins and insertions (hereafter collectively called muscle attachments).

Table 1: Measurability of Hill-type muscle architecture parameters across different measurement modalities.

Parameter	**MRI**	**Dissection**	**Handheld 3D scanning**
Fiber length (L_f)	Yes (DTI)	Yes	Yes (by tracing fibers)
Sarcomere length (L_s)	No	Yes (laser diffraction)	No
Pennation angle (θ_f)	Yes (DTI)	Yes	Yes (by tracing fibers)
Muscle volume (V_m)	Yes	Yes	No
Line of Action (LoA)	Yes	Yes, but unloaded*	Yes, but unloaded*
Insertion and origin	Yes	Yes	Yes
Joint Center of Rotation (JCR)	Yes	Yes, but unloaded*	Yes, but unloaded*

*In the unloaded ex vivo state, the lack of compression from body weight and muscle tone can cause a slight shift in the relative position of the bones and muscles compared to in vivo.

Dissection fixation methods

Validating in vivo imaging against a dissection gold standard presents a significant methodological challenge. The time-consuming nature of detailed dissection cannot be completed before an unfixed specimen degrades, making chemical fixation a necessity for tissue preservation. Standard practice involves preserving specimens through freezing or fixation. While some evidence suggests that short-term freezing minimally affects gross muscle architecture, traditional chemical fixatives like formalin, followed by ethanol storage, are known to significantly alter muscle mass and volume (14). The effect on muscle architecture parameters like fiber length remains unknown (7; 15; 14).

Recent developments have introduced alternative preservation methods to traditional formalin fixation. One such novel strategy is AnubiFIX™, used by the anatomy laboratory at the Erasmus Medical Centre. In contrast to conventional methods, AnubiFIX™ aims to preserve tissue in a state that more closely resembles fresh muscle by maintaining better tissue flexibility and plasticity (16). However, the quantitative effects of this new fixation method on muscle architecture have not yet been evaluated.

Without quantifying how a specific preservation method affects muscle architecture, researchers cannot determine whether discrepancies between fresh-tissue imaging and preserved-specimen dissection reflect true methodological differences or are simply preservation-induced artifacts. If these preservation effects are substantial, accelerating the dissection process could enable the analysis of fresh specimens, providing a more direct and reliable dataset for validating MRI results. Integrating new registration techniques, such as handheld 3D scanning and 3D digitizer measurements, into the dissection protocol offers a promising path to achieve this.

Aim

Therefore, the aim of this research was twofold: (1) to quantify the effects of AnubiFIX™ fixation on muscle volume by

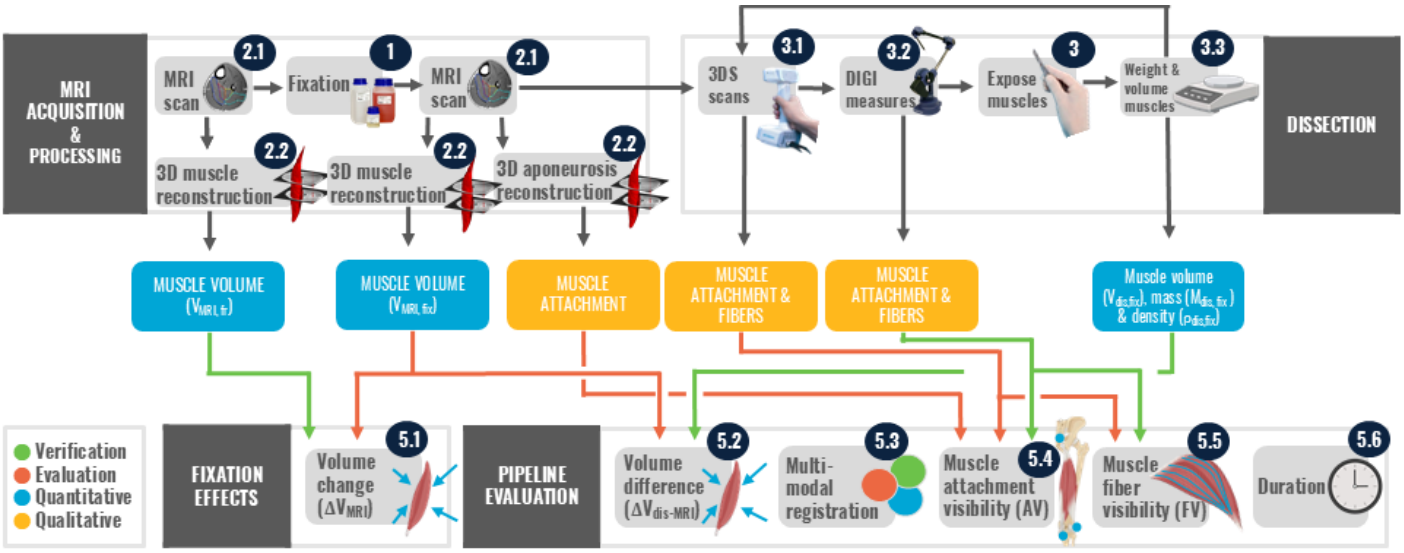

Figure 1: Schematic of the experimental pipeline and the derivation of muscle parameters from the measuring systems. MRI acquisition started with MRI scanning a fresh specimen (17), followed by fixation (16) of the tissue and a second MRI scan (17) to assess fixation effects. Muscle and aponeurosis segmentations from MRI data were reconstructed into 3D surface models (18). Dissection measurements started with handheld 3D scanning (19) of muscle surfaces and afterwards 3D digitizer measurements (20). Systematically, new muscles were exposed (21) by excising superficial muscles, after which they were weighed and the volume measured (22). The experimental pipeline was evaluated for aim 1 (fixation effects) and aim 2 (pipeline evaluation) through several measures. These included a validation of MRI-derived muscle volume against physical measurements, and a verification of handheld 3D scannings ability to visualize muscle fibers (22) and attachments (22). The practical feasibility of the pipeline was tested through multi-modal registration of the MRI 3D models, 3D scans (3DS) and 3D digitizer measurements (DIGI); and the duration of each step (22). Color-coded lines represent the study's analytical pathways: quantitative verification (green) and the evaluation of new fixation/measurement methods (red). Color-coded boxes represent the type of data produced: quantitative variables (blue) and qualitative variables (yellow). Dark blue circles: the section of the methodology where the step is explained.

comparing MRI data from fresh and fixated specimens, and (2) to develop a novel dissection pipeline integrating new registration techniques, handheld 3D scanning and 3D digitizer measurements, to measure muscle fibers and attachments rapidly, for validating MRI-derived muscle parameters. This work serves as a proof-of-principle study, designed to demonstrate the pipeline's feasibility and identify key challenges for future efforts to validate MRI-derived muscle parameters for musculoskeletal models.

2. Method

Our experimental pipeline, depicted in Figure 1, was implemented on both legs of a single human specimen, with bilateral measurements treated as two independent datasets (n=2 for each stage of data acquisition). This integrated approach combined ex vivo MRI scans (in both fresh and fixated states) with a dissection protocol enhanced by handheld 3D scanning and 3D digitizer measurements, allowing to address the aims directly. The fresh-versus-fixed MRI scans provided the data for aim 1, while the fixated MRI scans and multi-stage dissection process served as the basis for aim 2. To ensure data quality, we performed two verification checks: physically measured volumes of dissected muscles confirmed the accuracy of MRI-derived volumes, and 3D digitizer measurements verified the feasibility of the handheld 3D scanner. For the latter, we used 3D digitizer measurements of muscle attachments and muscle fibers. Since the traced path of a muscle fiber determines both L_f, and its θ_f, the successful tracing of fibers was used to evaluate the scanner's ability to capture the muscle fiber architecture parameters.

2.1. *Specimen preparation*

One (n=1) fresh-frozen human specimen of a 76-year-old male (body length: 176 cm, weight: 57 kg) was obtained from the Anatomy Department, Erasmus Medical Center, Rotterdam, Netherlands. The donor had provided written consent for their body to be used for science, and the study protocol was approved by the local ethics committee before its start. In accordance with Dutch law and institutional ethics committee requirements, no other forms of documentation were necessary.

The specimen was checked for the absence of lower-limb prosthetics. The specimen underwent initial MRI scanning after which it was pre-rinsed with AnubiFIX™ and afterwards fixated with formaldehyde (4.4%) for 1 week. During transport between facilities, the specimen was sealed in containers to maintain tissue hydration.

2.2. *MRI acquisition & processing*

2.2.1. *Acquisition*

MRI imaging was performed using a 3-T MRI scanner (Signa Premier; GE Healthcare) at the Radiology Department of Erasmus Medical Center, Rotterdam, Netherlands. Two scanning sessions were conducted with a 7-day interval: one before fixation of the fresh specimen ($\text{MRI}_{\text{fresh}}$) and one after fixation ($\text{MRI}_{\text{fixated}}$). Scans were acquired bilaterally in both supine and prone positions, covering the lower extremities from the L1 lumbar vertebral level to the feet.

The settings for the scan were: LAVA flex sequence, TR/TE 4.592/2.026 ms, field of view (FOV) 500 mm, acquisition matrix 420 × 500 mm (reconstructed to 512 × 512), voxel size 0.9766 × 0.9766 × 1 mm, and scan time 17 minutes and 40 seconds. This two-point fat quantification mDixon protocol enabled simultaneous acquisition of water and fat images for comprehensive muscle-aponeurosis differentiation. $MRI_{fixated}$ had a longer TR time of 4 milliseconds to account for the lower signal intensity. The scan resolution in both scans was chosen to balance image quality with a scan time suitable for future in vivo studies. For more detailed MRI settings see Appendix G.

To ensure consistent positioning in all supine MRI scans and dissection measurements, foam wedges were placed under the ankle and calf to maintain anatomical leg positioning (0° exorotation, flexion, and adduction of the hip and knee). This positioning prevented the thigh from contacting the MRI table, avoiding muscle compression from the leg's weight. The same standardized positioning was maintained during subsequent dissection procedures to ensure comparability between MRI scans and physical measurements. In the prone position, a foam wedge was placed between the feet to prevent the legs from exorotation. The angles of the joints were checked visually.

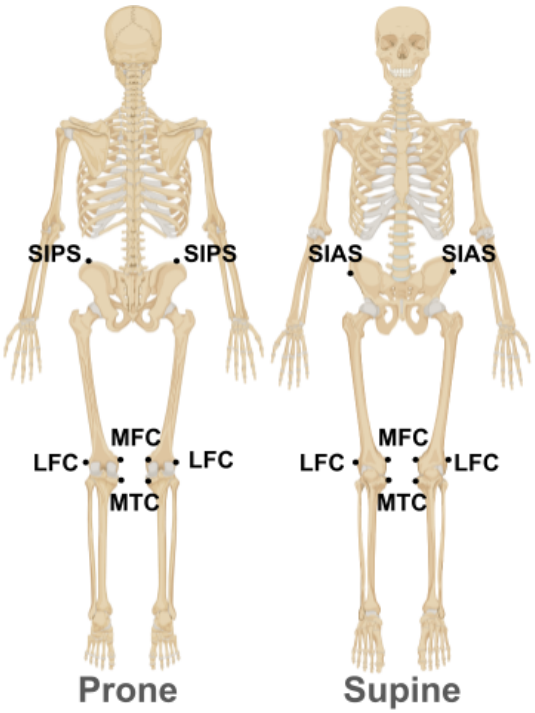

Figure 2: Location of the five bony landmarks (SIPS, SIAS, LFC, MFC, MTC) used for co-registration between MRI and dissection data. Skeleton images adapted from Biorender (22).

Before the second MRI session, oil capsules were placed on the skin at five bony landmarks (Fig. 2) as markers to facilitate multi-modal registration in section 2.4. These landmarks included the bilateral Spina Iliaca Posterior Superior (SIPS) and Spina Iliaca Anterior Superior (SIAS), and the unilateral lateral and medial femoral condyles (FLC, FMC) and tibial medial condyle (TMC). The SIAS and SIPS were included to anchor the pelvis and proximal femur, as internal landmarks such as the hip joint center or femoral head could not be directly accessed or instrumented without invasive procedures.

2.2.2. Segmentation

The muscles from Table 2, bones (femur, tibia, fibula, sacrum, lumbar vertebrae, hip bone), and oil capsule markers were outlined on all MRI slices where they were visible, using 3D Slicer (23). A specific protocol was developed for the origin and insertion aponeuroses due to the significant challenge of segmenting these thin, sheet-like structures. Particularly near the bone, the MRI signal was low, making the aponeurosis difficult to distinguish. Therefore, the segmentation strategy focused on identifying the distinct aponeurosis-tendon junction and then tracing the tendon as far as it was visible towards its bony attachment. For the muscle and bone models, an initial automatic segmentation was performed using the MuscleMap and TotalSegmentator Toolbox (24; 25; 26) on the out-of-phase mDixon MRI data. These annotations were manually reviewed, and afterwards refined using a gaussian smoothing filter (standard deviation 2.00 mm). All segmentations were made independently by the same experimenter with a total of three manual revisions of the segmentations.

From the segmentations, 3D triangulated surface models were created for all compartments using the MATLAB-based iso2mesh toolbox (27). From the 3D surface models of the muscles of both MRI_{fresh} and $MRI_{fixated}$ scans, muscle volumes were calculated ($V_{MRI_{fr}}$ and $V_{MRI_{fix}}$).

To ensure an accurate and stable alignment between datasets, a rigid transformation was performed using the bony landmarks as a reference, identified via the centroids of the 3D models of the oil capsule markers. This bone-based approach was specifically chosen to avoid alignment errors that could arise from using deformable soft tissues. The complete registration procedure is detailed in section 2.4.

*2.3. **Dissection protocol***

Muscles were progressively dissected per visible layer, following the systematic exposure sequence detailed in Table 2. This systematic approach ensured complete exposure of each muscle for accurate handheld 3D scanning and digitizer-based measurements. All measurements were performed bilaterally.

2.3.1. Handheld 3D scanning (3DS)

A handheld 3D scanner (EinScan H2; Shining 3D, Hangzhou, China) operated in white light mode, was used to create a 3D surface scan per dissection layer. Surgical drapes were positioned under the body to minimize reflective artifacts. The oil capsules placed at the bony landmarks during MRI, were replaced with pins with matte wooden caps for 3D scanner detection. Per leg and dissection layer from Tab 2, multiple 3D scans were recorded from mid-tibia until mid-thorax. These multiple scans were then merged using the EinScan H2 scanner's integrated software for automatic alignment. The volumetric accuracy, which reflects accumulated error across alignment and merging, is specified as 0.05±0.01 mm/m, resulting in

Table 2: Systematic muscle dissection by position, layer, and muscle group

Position	Layer	Muscle
Prone	1	Gluteus maximus (GMax), Semitendinosus (ST), Biceps femoris long head (BFlh)
	2	Gluteus medius (GMed), Semimembranosus (SM), Biceps femoris short head (BFsh)
	3	Gluteus minimus (GMin)
Supine	1	Rectus femoris (RF), Sartorius (SAR), Tensor fasciae latae (TFL)
	2	Vastus lateralis (VL), Vastus medialis (VM)
	3	Vastus intermedius (VI)
	4	Adductor longus (AL), Adductor brevis (AB), Gracilis (GRA), Pectineus (PEC)
	5	Psoas major (PM), Iliacus (IL), Adductor magnus (AM)

an expected error of approximately 0.13 mm over the scanned distance of approximately 0.75 m. Scan completeness was verified in real-time using the scanner's preview function. Failed merged scans were immediately repeated to ensure data quality. The bony landmarks (Fig. 2) were visually identified and annotated on the final 3D surface of the scan (3DS) to facilitate multi-modal registration in section 2.4.

2.3.2. 3D digitizer measurements (DIGI)

A 3D spatial digitizer (MicroScribe G2X; Immersion Corp., San Jose, CA, USA) was connected to a laptop to measure the location of the bony landmarks (Fig. 2), muscle origins and insertions, and the lengths of 10 muscle fibers per muscle in Rhino 8 (28). Each marker (matte wooden cap) was measured on both opposite sides, and the mean of these measurements was taken to represent the marker's center location to facilitate multi-modal registration in section 2.4. For each muscle origin and insertion, the digitizer captured the attachment geometry as individual points, multiple points, individual lines, or multiple lines, depending on the anatomical shape of the attachment site (Appendix I). The tip of the digitizer was run along the surface of the aponeurosis and from origin to insertion of clearly visible fiber bundles while recording the 3D coordinates of the tip. The recorded points were connected by polylines representing the muscle fibers.

2.3.3. Muscle volume and weight measurements

After removing the muscles to expose the deeper layers, each muscle was weighed ($M_{dis_{fix}}$) using a scale. The volume of the muscle ($V_{dis_{fix}}$) was calculated by subtracting the volume of water added from 1L (1000 mL), leveraging the fact that the density of water is 1 g/mL. The density of the muscles ($\rho_{dis_{fix}}$) was calculated from the measured dissected mass ($M_{dis_{fix}}$) and volume ($V_{dis_{fix}}$) as $\rho_{dis_{fix}} = \frac{M_{dis_{fix}}}{V_{dis_{fix}}}$ $[\frac{g}{cm^3}]$. This procedure was repeated for every muscle from Table 2.

2.4. Multi-modal co-registration

Data from MRI, 3DS, DIGI were captured in independent coordinate systems, making direct comparison difficult. Therefore, the purpose of multi-modal co-registration was to align all datasets within a common reference frame defined by the MRI data. By transforming both the 3DS and DIGI datasets into the MRI's coordinate space, all datasets could be spatially overlaid. This alignment process enabled two key objectives: 1) to allow for visual comparison of muscle fibers between 3DS and DIGI (3DS-DIGI), 2) visual comparison of muscle attachments between 3DS and DIGI (3DS-DIGI), and 3) to quantitatively assess the residual misalignment between the markers in MRI, 3DS and DIGI (3DS-DIGI, 3DS-MRI), thereby verifying the accuracy of the integration of the data of MRI, 3DS and DIGI.

Rigid body transformations were computed to best align the 3DS marker set with the corresponding MRI marker set (3DS-MRI). Separate transformations were similarly computed to align the 3D digitizer marker set with the 3DS marker (3DS-DIGI). Each transformation was calculated to minimize the least squares distance between the corresponding marker sets using the algorithm by Söderkvist & Wedin (29).

2.5. Pipeline evaluation metrics

This section evaluates the proposed pipeline of this study (Fig. C.12) through quantitative and qualitative measures. First, to quantify the effects of fixation (aim 1), the volumetric change between fresh and fixated MRI scans was calculated. Second, to test the dissection workflow (aim 2), four performance metrics were used for its evaluation: the verification between MRI-derived and physically measured volumes, the accuracy of the multi-modal co-registration, the qualitative visibility of muscle fibers and muscle attachments on 3D scans, and the duration of the pipeline's workflow. The analyses were performed in MATLAB version R2024B and Blender 4.4 (see Appendix S for details).

2.5.1. Fixation induced muscle volume change

The effect of fixation on muscle volume was quantified by comparing the muscle 3D models reconstructed from the $\text{MRI}_{\text{fresh}}$ versus $\text{MRI}_{\text{fixated}}$. This analysis used only the supine MRI scans because the foam wedges prevented muscle compression from the leg's weight and provided more consistent positioning between scans. This ensured that any observed changes were due to fixation effects rather than positional deformation. The percentage volume change for each muscle between MRI scans was calculated using the formula: $\Delta V_{MRI} = \frac{V_{MRI_{fix}} - V_{MRI_{fr}}}{V_{MRI_{fr}}} \cdot 100\%$. The mean percentage volume change and standard deviation of this mean represented the overall volumetric effect of fixation on the muscles.

2.5.2. Dissection volume verification

To verify the accuracy of the MRI-derived 3D models of the muscles with dissection, we performed two checks. First, agreement between the $V_{dis_{fix}}$ and $V_{MRI_{fix}}$ was assessed using a Bland-Altman analysis, as muscle volume measurements were performed on the fixated, excised muscles. Individual muscle

volume differences ($\Delta V_{dis-MRI_{fix}} = V_{MRI_{fix}} - V_{dis_{fix}}$ [cm^3]) were additionally reported.

To verify the adequate removal of non-muscular tissue, this $\rho_{dis_{fix}}$ was compared against the literature value of 1.12 [$\frac{g}{cm^3}$] for fixated muscle (30). The mean difference ($\Delta\rho_{dis_{fix}}$) and standard error between the measured densities and this literature value represented the accuracy of the volume dissection ($V_{dis_{fix}}$) measurements.

2.5.3. Multi-modal registration accuracy

The accuracy of each resulting alignment was evaluated by quantifying the residual errors using two complementary metrics:

- *Positional deviation*, quantified as the *Root Mean Square Error (RMSE)*. This metric represented the average euclidean distance remaining between corresponding landmarks after the transformation was applied. This calculation was done for all markers locations in both prone and supine position of 3DS-MRI and 3DS-DIGI.

- *Rotational deviation*, quantified as the *Mean Angular Deviation (MAD)*. This metric represents the final angular misalignment of the coordinate frames per leg (left and right). Singular Value Decomposition (SVD) was applied to the 3DS marker set and the aligned marker sets of MRI and DIGI, with the rotation matrix **R** decomposed into Euler angles: roll (X), pitch (Y), and yaw (Z). To ensure anatomical interpretability, the SVD-derived axes were reordered such that roll corresponded to rotation about the anterior–posterior axis, pitch to rotation about the medio–lateral axis, and yaw to rotation about the proximal–distal axis. The overall angular misalignment between these 3 axes was summarized as the Mean Angular Deviation (MAD) for 3DS-MRI and 3DS-DIGI.

2.5.4. Muscle fiber and attachment visibility

The visibility of muscle fibers and muscle attachments in 3DS was qualitatively assessed using the co-registered DIGI measurements as the ground-truth verification. The evaluation was performed as follows:

- **Muscle fibers**: visibility of muscle fibers on the 3DS scans was categorized as 'visible' or 'not visible', a binary outcome recorded as the variable Fiber Visibility (FV). A 'visible' classification required that individual fiber bundles could be clearly distinguished and traced. This was verified by confirming their correspondence with the overlaid DIGI fiber polylines.

- **Muscle attachments**: The visibility of origins and insertions on the 3DS scans were also categorized as 'visible' or 'not visible'. An attachment was classified as 'visible' if its boundaries could be clearly delineated on the 3DS scan and this outline corresponded with the perimeter of the DIGI measurements. This assessment was performed independently for origins (AV_O) and insertions (AV_I).

To assess the possibility of MRI-derived aponeurosis-tendon models to estimate the location of muscle attachment to the bone, a secondary qualitative comparison was made with the dissection data (3DS and DIGI). This visual analysis focused on areas where the MRI-derived aponeurosis-tendon 3D models and the physically observed muscle attachments in 3DS and DIGI shared a similar, well-defined geometry, and was reported descriptively.

2.5.5. Pipeline duration

The duration of each procedure from "MRI acquisition & processing" and "Dissection protocol" was recorded every 15 minutes to assess the practical feasibility of the integrated pipeline. 3DS represents the "new" imaging-based workflow, while DIGI measurements, volume, and weight assessments represented the state-of-the-art dissection approaches. Comparing the time required for 3DS to that of DIGI, volume, and weight measurements allowed evaluation of the efficiency of the new pipeline relative to standard dissection methods.

3. Results

Individual muscle measurements are summarized in Table 3. During dissection, the left semitendinosus muscle was discovered to be torn in half and was therefore excluded from the digitizer measurements due to complete damage to both the muscle fibers and tendon. The left semimembranosus had a small tear, which did not compromise its in situ location and was therefore still included.

3.1. Fixation induced muscle volume change

The mean of ΔV_{MRI} between the $V_{MRI_{fr}}$ and $V_{MRI_{fix}}$ was 31.51% (SD±23.32%). This indicated that muscle volumes became larger, once they had been fixated with AnubiFIX™ fixation.

3.2. Dissection volume verification

Bland-Altman analysis between the $V_{dis_{fix}}$ and $V_{MRI_{fix}}$ revealed a systematic bias of +48.13 cm^3 (SD 52.84 cm^3) (Fig. 3), with $V_{MRI_{fix}}$ consistently larger than $V_{dis_{fix}}$. Two measurements fell outside the 95% limits of agreement (−55.44 to +151.70 cm^3). The plot also indicated a proportional bias, where the absolute difference between measurement methods tended to increase with the average muscle volume.

The mean $\rho_{dis_{fix}}$ of all twenty muscles was 1.36 g/cm^3 (SD 0.23 g/cm^3). These densities differed from the literature value of 1.12 g/cm^3 with a mean and standard error of $\Delta\rho_{dis} = 0.24 \pm 0.04$ g/cm^3.

3.3. Multi-modal registration accuracy

The co-registration errors of the integration of MRI, 3DS and DIGI are reported as the positional error per marker and as the rotational error per rotational axis in the Table 4. A depiction of the MRI, DIGI and 3DS data is shown in Fig. 4, with the respective co-registration of these data.

Table 3: Muscle architectural parameters grouped by limb. For both the left (L) and right (R) leg, the table lists dissected mass ($M_{dis_{fix}}$), volume ($V_{dis_{fix}}$), and calculated density (ρ), alongside volumes from fresh ($V_{MRI_{fr}}$) and fixated ($V_{MRI_{fix}}$) MRI scans. Calculated differences include the percentage volume change due to fixation (ΔV_{MRI}) and the absolute volume difference between fixated MRI and dissection ($\Delta V_{dis-MRI}$). Qualitative data includes muscle fiber visibility (FV) and attachment visibility for origins (AV_O) and insertions (AV_I): Y = Yes, N = No.

	Left Leg							Right Leg							3DS visibility		
Muscle	$M_{dis_{fix}}$ [g]	$V_{dis_{fix}}$ [cm^3]	ρ [$\frac{g}{cm^3}$]	$V_{MRI_{fr}}$ [cm^3]	$V_{MRI_{fix}}$ [cm^3]	ΔV_{MRI} [%]	$\Delta V_{dis-MRI}$ [cm^3]	$M_{dis_{fix}}$ [g]	$V_{dis_{fix}}$ [cm^3]	ρ [$\frac{g}{cm^3}$]	$V_{MRI_{fr}}$ [cm^3]	$V_{MRI_{fix}}$ [cm^3]	ΔV_{MRI} [%]	$\Delta V_{dis-MRI}$ [cm^3]	**FV**	**AV_O**	**AV_I**
RF	150	113	1.33	115	130	13.5	17	150	109	1.38	124	146	17.5	37	Y	N	Y
SAR	99	72	1.38	47	84	77.5	12	106	68	1.56	58	100	72.4	32	N	Y	N
TFL	86	64	1.34	62	71	15.7	7	84	44	1.91	56	60	7.7	16	Y	Y	N
VL	362	315	1.15	371	396	6.7	81	537	490	1.10	396	416	5.0	-74	Y	Y	Y
VM	383	323	1.19	258	353	36.7	30	353	327	1.08	289	401	38.7	74	Y	N	Y
VI	284	243	1.17	230	319	38.6	76	227	180	1.26	276	385	39.4	205	N	N	N
AL	92	50	1.84	85	95	11.8	45	94	58	1.62	103	87	-15.7	29	N	Y	N
GRA	59	40	1.48	28	56	96.8	16	63	37	1.70	47	53	12.1	16	Y	Y	Y
PEC	29	19	1.53	20	24	22.0	5	24	18	1.33	18	22	22.4	4	N	Y	N
AB	18	20	0.90	50	53	4.9	33	69	43	1.60	41	48	18.0	5	N	Y	N
AM	415	359	1.16	354	490	38.4	131	324	282	1.15	340	419	23.5	137	Y	N	Y
PM	182	142	1.28	108	149	38.1	7	154	105	1.47	134	158	17.9	53	N	N	N
IL	124	83	1.49	142	138	-2.6	55	144	105	1.37	123	163	32.8	58	Y	N	N
GMax	953	891	1.07	741	885	19.3	-6	882	833	1.06	683	839	22.9	6	Y	Y	N
GMed	350	293	1.19	323	470	45.5	177	348	301	1.16	277	431	55.5	130	Y	N	N
GMin	109	83	1.31	101	150	49.3	67	123	98	1.26	105	155	47.3	57	Y	N	N
BFlh	141	110	1.28	102	147	43.4	37	134	85	1.58	90	121	35.7	36	N	N	Y
ST	114	85	1.34	94	112	19.0	27	124	82	1.51	81	110	35.3	28	N	N	Y
BFsh	88	56	1.57	67	85	27.0	29	80	46	1.74	53	74	38.5	28	N	N	Y
SM	212	170	1.25	153	276	80.2	106	194	140	1.39	155	236	51.9	96	N	N	N

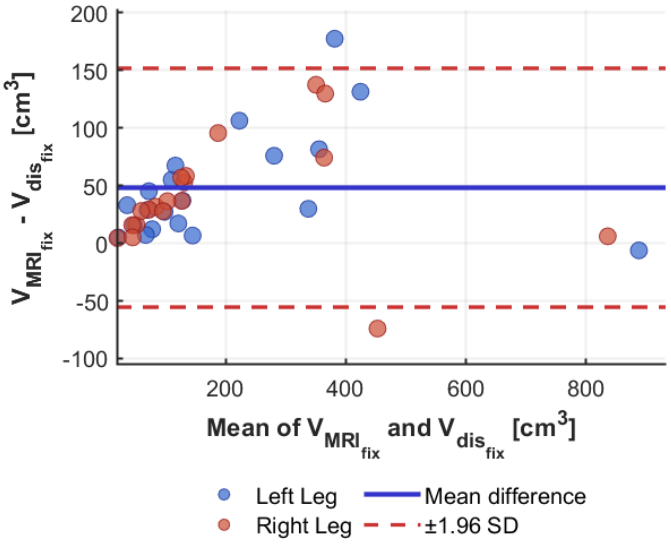

Figure 3: Bland-Altman plot comparing muscle volume measurements between measured volume during dissection ($V_{dis_{fix}}$) and fixated ($V_{MRI_{fix}}$)) MRI acquisitions. Each point represents a single muscle from the left (blue) or right (red) leg (n = 40). The plot shows the mean difference (solid blue line) and limits of agreement (±1.96 SD, dashed red lines) between the two measurement conditions.

3.4. Muscle fiber and attachment visibility

In 50% of the muscles, muscle fibers were visible on the 3DS scans. In the other 50% of muscles, the fibers were not well traceable (see Appendix O & Appendix P for details).

Of the 20 muscles analyzed, 8 (40%) demonstrated clearly visible origins in the 3DS scans that corresponded with the DIGI point perimeters. These included superficial muscles originating from prominent bony landmarks such as SAR, TFL, and GMax from the iliac spine and crest, VL from the greater trochanter and linea aspera, and the adductor group (AL, AB, GRA, and PEC) from the pubic rami. Seven muscles (35%) displayed clearly visible insertions in the 3DS scans. These comprised the quadriceps group (RF, VL, VM) inserting via the patellar tendon to the tibial tuberosity, hamstring muscles (BFlh, ST, BFsh) with distinct insertions on the fibular head and pes anserinus, GRA at the pes anserinus, and AM at the adductor tubercle. Origins and insertions that were not clearly distinguishable in the 3DS data, often had a deep anatomical position, making them inaccessible in superficial layers (e.g., VI, PM, IL, GMed, GMin, SM); or possessed broad, diffuse attachment areas lacking distinct boundaries (e.g., the origins of RF, VM, AM, BFlh, BFsh, ST; and the insertions of SAR, TFL, GMax, AL, AB, PEC).

The visual overlay of MRI-derived aponeurosis-tendon models with the dissection data (3DS and DIGI) revealed poor correspondence because the 3D MRI-derived models were difficult to compare with the 3D surface data of 3DS and DIGI. Where 3DS and DIGI could only provide muscle attachment data from

Table 4: Marker positioning errors and axes deviation for the three types of co-registered markers (MRI, 3DS, and DIGI measurements). 3DS-DIGI: the error of the co-registration of the 3DS markers and the DIGI measurement for each individual muscle. 3DS-MRI: the error of the co-registration of the MRI and 3DS markers per dissection layer. n: the number of marker or axis pairs analyzed.

		n	3DS-DIGI	n	3DS-MRI
Marker	**Prone**		**RMSE ± SD (mm)**		**RMSE ± SD (mm)**
	SIPS	13	20.6 ± 13.7	6	21.5 ± 6.5
	LFC	13	30.1 ± 9.0	6	25.4 ± 10.3
	MFC	13	47.9 ± 9.6	6	33.6 ± 11.2
	MTC	13	41.6 ± 7.6	6	15.7 ± 5.8
	Supine		**RMSE ± SD (mm)**		**RMSE ± SD (mm)**
	SIAS	26	6.9 ± 7.3	10	13.2 ± 8.0
	LFC	26	19.4 ± 18.9	10	19.5 ± 5.0
	MFC	26	24.5 ± 21.6	10	36.9 ± 11.2
	MTC	26	19.0 ± 13.1	10	35.7 ± 10.3
Axis			**MAD ± SD (°)**		**MAD ± SD (°)**
	Roll (X)	39	0.9 ± 1.0	16	1.1 ± 0.7
	Pitch (Y)	39	1.4 ± 2.6	16	2.7 ± 3.8
	Yaw (Z)	39	2.0 ± 2.6	16	3.1 ± 3.6

Table 5: Time breakdown of the experimental pipeline, split into two possible workflows. New: representing the researched potential of using 3DS in dissection pipeline. State-of-the-art: the current dissection validation method using DIGI and manual measurement.

Phase methodology	**Person-hours**	
	New	**State-of-the-art**
MRI acquisition & processing		
MRI scanning	3.0	3.0
MRI segmentation	117.0	117.0
Subtotal MRI	*120.0*	*120.0*
Dissection		
Exposing new muscle	31.0	31.0
3DS	3.5	-
Remove and measure muscle volume and weight	-	25.0
DIGI	-	14.5
Subtotal Dissection	*34.5*	*70.5*
Total person-hours	**154.5**	**190.5**

the top surface of the dissected legs, the MRI aponeurosis-tendon models indicated the full 3D surface of the aponeurosis-tendon complex. This made direct comparison between the two impossible because they each measured the origins and insertions inherently different.

3.5. Duration

The time requirements for the entire experimental pipeline are detailed in Table 5, comparing the newly investigated 3DS method with the established DIGI approach for dissection validation. The complete pipeline required 154.5 person-hours when using the new 3DS registration method, compared to 190.5 person-hours with the state-of-the-art DIGI approach, a 36-hour reduction that demonstrates the efficiency potential of 3DS. A detailed breakdown of the duration of each step per dissection layer is reported in Appendix K.

The most time-intensive component remained MRI segmentation at 117 person-hours, representing the total time investment regardless of the dissection registration method.

The primary time savings of the pipeline occurred during the dissection phase. The rapid surface capture by 3DS (3.5 hours) was to replace both the time-intensive manual digitization with the DIGI (14.5 hours) and the physical procedures for measuring muscle volume and weight (part of the 25-hour task). However, the "new" dissection workflow's subtotal in Table 5 does not account for the time required to remove muscles to access deeper layers, a step necessary in both workflows. By estimating that muscle removal constitutes approximately 10 hours of the 25-hour "remove and measure" task in the "state-of-the-art" workflow, the more realistic potential for reducing dissection time by using 3DS is estimated at 15–20 person-hours.

4. Discussion

The aim of this study was two-fold; first we wanted to understand the effects of fixation on MRI-derived muscle volume, and second we wanted to test the feasibility of new registration technologies 3DS and DIGI to make dissection studies more accurate and fast. We proposed an integrated approach combining ex vivo MRI scans (in both fresh and fixated states) with a dissection protocol enhanced by handheld 3D scanning and 3D digitizer measurements, allowing us to address our aims directly.

We found that AnubiFIX™ fixation induced a substantial average muscle volume increase of 31.5%, a critical finding for imaging studies seeking to validate their method on fixated muscle.

The verification of the dissection procedure showed that $V_{MRI_{fix}}$ systematically exceeded $V_{dis_{fix}}$ by 48.1 cm^3. While the multi-modal registration demonstrated promising rotational accuracy (MAD $< 3°$), it was limited by substantial positional errors (RMSE 6.9 – 47.9 mm). 3DS demonstrated limited capability for capturing muscle architecture, visualizing muscle fibers in 50% of the muscles, and visualizing 40% of origins and 35% of insertions of the muscles. Despite this, the 3DS offered a significant practical benefit, with an estimated potential to reduce dissection time by 15–20 person-hours.

In the following sections, each of these five findings is subsequently elaborated upon. We will address the multi-modal registration last, as it represents a methodological step required for our comparisons, rather than a direct outcome related to the study's primary aims.

4.1. Fixation induced muscle volume change

In our findings we quantified the magnitude of the change in muscle volume after fixation, revealing a mean muscle swelling of ΔV_{MRI} = 31.51 (SD ±23.32%). This substantial change is consistent with historical observations of 25–50% volume increases in muscles fixed in situ on the skeleton during early post-mortem stages (31), after which they often shrink. However, the most critical finding is not the average swelling, but

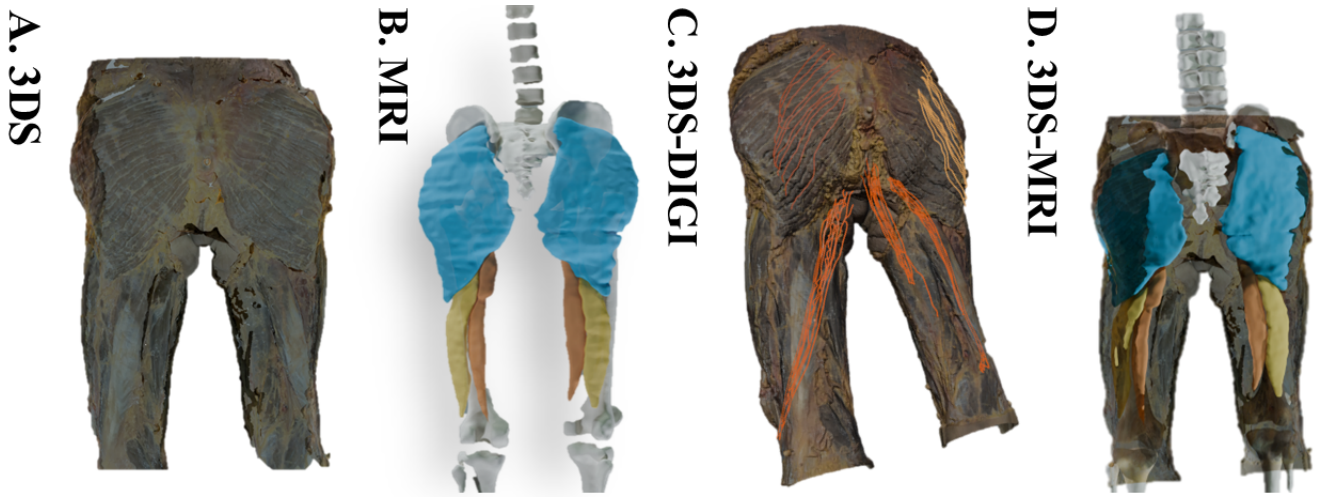

Figure 4: A) 3DS in prone position, dissection layer 1. B) The MRI 3D model of the muscles and bones in prone position, dissection layer 1. Muscles, GMax (blue), ST (orange) and BFlh (yellow). C) Co-registered 3DS-DIGI, showing muscle fibers in prone position, dissection layer 1. D) Co-registered 3DS-MRI, showing the data of image A and B combined. In B & D the thigh and leg bones are also modeled and aligned to give anatomical perspective.

its high variability between muscles (SD ±23.32%). To our knowledge, this study is the first to report these significant inter-muscle differences because, until now, research investigating fixation-induced muscle changes predominantly relied on traditional muscle volume measurements that obscure this phenomenon. These methodologies, involve dividing whole muscles into small, homogenous samples for analysis and serve as ground truth for the effect fixation has on muscle volume and density, (32; 30; 33). This sample processing strategy, by its very nature, makes it impossible to assess the unique response of an individual, intact muscle, as it averages out the intra-muscle differences. This variability between muscles demonstrates that fixation does not produce a uniform, predictable change across all muscles. Factors such as initial tissue hydration, fat content, and anatomical location likely influence each muscle's specific response (30). This variability makes a simple mathematical correction unfeasible and highlights the danger of assuming a consistent fixation effect. Measuring these changes on muscles within an experimental pipeline, as our MRI-based approach allows, may provide the direct, quantifiable data needed to account for this variable effects.

4.2. Dissection volume verification

A primary finding of our dissection workflow was the systematic difference between V_{MRIfix} and $V_{dis_{fix}}$. The elevated mean density of the dissected muscles (1.36 ± 0.23 g/cm^3 vs. a literature value of 1.12 g/cm^3) strongly indicates that tissue dehydration was the primary cause. This density increase is the expected physical outcome, as the evaporation of water, which is less dense than the remaining muscle tissue, leaves behind a denser material. This interpretation is also supported by the visible signs of tissue dehydration noted over during the dissection procedure.

Furthermore, the timing of the dissection appears to have introduced a dynamic variable into this process, underscoring the inadequacy of a single textbook density value. We observed that the magnitude of the volumetric error was related to the dissection sequence; for instance, the GMax was the first muscle excised and showed a smaller volume discrepancy than muscles excised and measured on later days. This suggests that the density of the tissue changed progressively throughout the experiment, deviating further from the standard value as muscles were exposed to air for longer periods.

The Bland-Altman analysis also revealed a clear proportional bias where larger muscles showed greater discrepancies. This is likely related to the anatomical attachment and position of larger muscles. Larger muscles often have more extensive and complex attachment areas, making complete removal more challenging. This is because smaller muscles more often have cord-like tendons that allow for a clean transection from the bone, whereas larger muscles frequently have broad aponeuroses or originate directly from the bone's periosteum, making a complete and clean excision practically impossible. A clear case was the VI, which originates directly from the femur shaft.

Inaccurate MRI segmentation of muscles that often lay deep and are largely intertwined with their neighbors, such as the VI and GMed, may have contributed to this proportional effect too. For these muscles, defining a clear border for both MRI segmentation is difficult, likely contributing to the largest observed deviations. This can be seen in the difference in volume of these muscles between the right and left leg. The observed differences between the left and right leg in the gluteal and vastii muscles were excessively large in $V_{MRI_{fix}}$. The VI showed the largest asymmetry (66 cm^3 difference between legs), followed by VM (48 cm^3), GMax (46 cm^3), and GMed (39 cm^3). Such substantial bilateral differences exceed what would be expected from normal anatomical variation, indicating that the MRI segmentation of these muscles might not have been as accurate. Another factor that most likely contributed to this is the inexperience of the researcher who segmented these muscles. In future studies, employing multiple researchers with more ex-

perience in muscle segmentation could minimize segmentation errors and improve measurement reliability.

4.3. Muscle fiber and attachment visibility

The evaluation of 3DS as a measurement tool revealed that the visibility of muscle fibers and attachments was frequently compromised. This was due to several technical limitations. First, as a purely optical method, a 3DS scan cannot replicate the crucial tactile feedback of palpation often used in manual dissection to define muscle attachment borders that are not visually distinct. Second, 3DS can capture the surface, but it provides no information about internal fiber architecture. And third, the anatomical environment itself posed challenges, such as strong reflection artifacts on wet surfaces that obscured surface detail. Beyond these scanner-specific issues, the challenge of tracing muscle fibers covered by fat or tendon highlights a more fundamental problem. This is not merely a limitation of 3DS but of the in-situ dissection approach itself, as traditional manual measurements face the same obstacle. So for the measurement of muscle fibers, the direct, tactile feedback of DIGI is likely more accurate as it allows for immediate, tactile measurement of L_f and θ_f.

However, for muscle attachments, 3DS shows significant potential if the methodology is adapted. Excising the muscle to fully expose the attachment site would allow for an unobstructed scan. Therefore, a valuable direction for future work is to use 3DS to capture these exposed attachment sites, while using the DIGI measurements to provide tactile verification of the attachment borders. This improved dissection-based registration, could then facilitate a more targeted and robust validation against the MRI-derived aponeurosis-tendon 3D models. Such a validation could not only assess the accuracy of the MRI models but could also provide the necessary data to improve their estimates, for instance, through predictive modeling.

For such a validation to be meaningful, however, the accuracy of the MRI-derived models themselves must also be considered. The segmentation of the aponeurosis-tendon complex proved to be difficult, as the thin aponeurotic sheets are challenging to delineate, especially near bony insertions where the MRI signal is weaker. To address this, the MRI scanning protocol should be optimized. While our study used mDixon MRI for excellent muscle delineation, T1-weighted MRI shows better promise to provide more precise segmentation of the aponeurosis-tendon complex (34). This is critical, as the aponeurosis determines muscle fiber termination and the tendon determines muscle attachment locations (35). Future musculoskeletal modeling should therefore consider a hybrid approach, integrating mDixon sequences for accurate muscle volume with T1-weighted imaging for superior aponeurosis definition. This would optimize the visualization of the entire muscle-tendon-bone unit.

4.4. Duration

Beyond the challenges of muscle fiber and attachment visibility in 3DS, the dissection workflow's practical feasibility also depends on its efficiency. Our analysis confirms that while 3DS improves data capture speed, this gain is insufficient to overcome the muscle degradation. The most time-consuming preparatory stages, the meticulous removal of fat and fascia to expose muscles, still take several days - far exceeding degradation window of fresh tissue. This confirms that post-imaging fixation remains an unavoidable step when validating MRI against dissection gold standards, as the specimen must be chemically preserved after fresh imaging to prevent degradation during the subsequent multi-day dissection process.

While 3DS offered rapid data capture, its overall capability for measuring muscle fibers and attachments is questionable. Besides the limitations of 3DS described in the previous section, muscle fibers and muscle attachments would still have to be traced on the surface of 3DS. So in comparison to DIGI, the determination of L_f, θ_f and muscle attachments, would still require manual, point-by-point tracing in the post-processing of 3DS (see Appendix Q for details), and thus likely not leveraging measurement efficiency. However, 3DS offers distinct advantages: it creates a permanent digital record enabling post-processing verification and retrospective quality control. Therefore, while DIGI may be more accurate and efficient for measurements of L_f, θ and muscle attachments, 3DS provides quick data preservation opportunities.

The most time-intensive part of the entire pipeline was manual MRI segmentation. Automated segmentation algorithms, which are typically trained on in vivo data, performed poorly on our ex vivo scans due to the altered image contrast resulting from the specimen's lower temperature and reduced MRI signal. This incompatibility made manual segmentation unavoidable for our study. However, since dissection-based validation studies inherently involve small sample sizes, typically only a few specimens for verification purposes, the time investment in manual segmentation, possibly improved through more experienced researchers, remains manageable.

4.5. Multi-modal co-registration accuracy

This study tested the feasibility of a marker-based system for integrating all MRI, 3DS and DIGI, and while the large positional errors (RMSE ranged from 6.9-47.9 mm) suggest a poor match, the consistently low angular deviations (MAD of $< 3.1°$) indicate that the relative orientation between the skeletal segments was accurately preserved. The significant positional discrepancies should therefore be interpreted as a direct consequence of the instability of the non-rigid, superficial markers used, which shifted due to soft tissue deformation and skin retraction. Despite these limitations, the preserved angular accuracy demonstrates that multi-modal registration holds potential for future studies aiming to co-register imaging and dissection data. For investigations that require precise localization between MRI and dissection, such as mapping muscle attachment

sites on bone surfaces, implementing more stable marker systems could substantially improve the co-registration accuracy between MRI, 3DS, and DIGI data.

5. Conclusion

This proof-of-principle study demonstrated that the validation of MRI-derived muscle parameters through dissection requires its own verification, as the process of fixation and dissection introduces volumetric muscle artifacts too substantial to be ignored. Our findings establish distinct roles for new technologies within this pipeline to measure muscle fibers and attachments: handheld 3D scanning as a tool for rapid digital documentation of dissection, while the 3D digitizer is the superior instrument for the measurement of muscle fibers and attachments. When precisely co-registered, this combination of handheld 3D scanning and 3D digitization creates an opportunity to improve the accuracy of muscle origin and insertion data derived from anatomical MRI. By providing a framework to understand the effects of fixation, dehydration, and measurement technology, this work takes a critical step toward enabling meaningful comparisons between MRI and dissection for musculoskeletal models.

Acknowledgments

This study was conducted as a Master's Thesis project for the Master's degree of Mechanical Engineering, specializing in Biomechanical Design. This research would not have been possible without the invaluable guidance of my supervisor, Eline van der Kruk. Her prompt responses, extensive constructive feedback, and unwavering enthusiasm made my last year truly a enjoyable experience. I am equally grateful to Bart Bolsterlee and Hilco Theeuwes for their mentorship and for generously providing access to their (laboratory) facilities throughout this past year.

Special thanks go to Claudia Kruissel at EMC, whose tireless support with every detail ensured my MRI and dissection proceeded smoothly. Finally, I extend my appreciation to the students at the EMC anatomic lab - Lucas, Esmee and Sjoerd - and to Martijn and Yoni from the Bodies lab. Your thoughtful discussions, generous time, and insights constantly challenged me to think more deeply about my work.

References

[1] Ajay Seth, Jennifer L Hicks, Thomas K Uchida, Ayman Habib, Christopher L Dembia, James J Dunne, Carmichael F Ong, Matthew S DeMers, Apoorva Rajagopal, Matthew Millard, Samuel R Hamner, Edith M Arnold, Jennifer R Yong, Shrinidhi K Lakshmikanth, Michael A Sherman, Joy P Ku, and Scott L Delp. OpenSim: Simulating musculoskeletal dynamics and neuromuscular control to study human and animal movement. *PLoS Comput. Biol.*, 14(7):e1006223, July 2018.

[2] Pauline Gerus, Guillaume Rao, and Eric Berton. Subject-specific tendon-aponeurosis definition in hill-type model predicts higher muscle forces in dynamic tasks. *PLoS ONE*, 7(8):e44406, 2012.

[3] Liliam Fernandes de Oliveira and Luciano Luporini Menegaldo. Individual-specific muscle maximum force estimation using ultrasound for ankle joint torque prediction using an emg-driven hill-type model. *Journal of Biomechanics*, 43(14):2816–2821, 2010.

[4] Frederik Heinen, Morten E. Lund, John Rasmussen, and Mark De Zee. Muscle-tendon unit scaling methods of hill-type musculoskeletal models: An overview. In *Proceedings of the Institution of Mechanical Engineers, Part H: Journal of Engineering in Medicine*, volume 230, pages 976–984. SAGE Publications Ltd, 10 2016.

[5] Bruce M. Damon, Martijn Froeling, Amanda K.W. Buck, Jos Oudeman, Zhaohua Ding, Aart J. Nederveen, Emily C. Bush, and Gustav J. Strijkers. Skeletal muscle diffusion tensor-mri fiber tracking: rationale, data acquisition and analysis methods, applications and future directions, 3 2016.

[6] Jos Oudeman, Aart J. Nederveen, Gustav J. Strijkers, Mario Maas, Peter R. Luijten, and Martijn Froeling. Techniques and applications of skeletal muscle diffusion tensor imaging: A review. *Journal of Magnetic Resonance Imaging*, 43(4):773–788, 2015.

[7] B Bolsterlee, T Finni, A D'Souza, J Eguchi, EC Clarke, and RD Herbert. Three-dimensional architecture of the whole human soleus muscle in vivo. *PeerJ*, 6, 4 2018.

[8] Stefan Papenkort, Markus Böl, and Tobias Siebert. Architectural model for muscle growth during maturation. *Biomechanics and Modeling in Mechanobiology*, 20(5):2031–2044, 2021.

[9] Henry Tregidgo, Adrià Casamitjana, Caitlin Latimer, Mitchell Kilgore, Eleanor Robinson, Emily Blackburn, Koen Van Leemput, Bruce Fischl, Adrian V. Dalca, Christine Mac Donald, Dirk Keene, and Juan Eugenio Iglesias. 3d reconstruction and segmentation of dissection photographs for mri-free neuropathology. *arXiv preprint*, 2009.05596, 2020.

[10] Mohd Javaid, Abid Haleem, Ravi Pratap Singh, and Rajiv Suman. Industrial perspectives of 3d scanning: Features, roles and it's analytical applications. *Sensors International*, 2:100114, 2021.

[11] Kerri L Colman, Hans H de Boer, Johannes GG Dobbe, Niels PTJ Liberton, Kyra E Stull, Maureen van Eijnatten, Geert J Streekstra, Roelof-Jan Oostra, Rick R van Rijn, and Alie E van der Merwe. Virtual forensic anthropology: The accuracy of osteometric analysis of 3d bone models derived from clinical computed tomography (ct) scans. *Forensic science international*, 304:109963, 2019.

[12] Dolores Messer, Michelle S. Svendsen, Anders Galatius, Morten T. Olsen, Vedrana A. Dahl, Knut Conradsen, and Anders B. Dahl. Measurement error using a seemalab structured light 3d scanner against a microscribe 3d digitizer. *PeerJ*, 9:e11804, 2021.

[13] Daniel Ehrhardt et al. Accuracy of handheld 3d scanners for capturing bone surface geometry: A comparative study. *Journal of Biomechanical Engineering*, 144(6):064501, 2022.

[14] Kaitlyn C. Leonard, Nikole Worden, Marissa L. Boettcher, Edwin Dickinson, and Adam Hartstone-Rose. Effects of freezing and short-term fixation on muscle mass, volume, and density. *The Anatomical Record*, 305(1):199–208, May 2021.

[15] Peter Agger, Thomas Lass, Morten Smerup, Jesper Frandsen, and Michael Pedersen. Optimal preservation of porcine cardiac tissue prior to diffusion tensor magnetic resonance imaging. *Journal of Anatomy*, 227(5):695–701, 2015.

[16] AnubiFix. Producten, 2025. Accessed: 2025-06-18.

[17] Bart Bolsterlee, Arkiev D'Souza, and Robert D Herbert. Reliability and robustness of muscle architecture measurements obtained using diffusion tensor imaging with anatomically constrained tractography. *J. Biomech.*, 86:71–78, March 2019.

[18] Meeghage Randika Perera, Pan Su, Samantha Holdsworth, and Geoffrey Handsfield. Changes to muscle and fascia tissue after eighteen days of ankle immobilization post-ankle sprain injury: an mri case study. *BMC Musculoskeletal Disorders*, 26(1), 2025.

[19] Shining 3D. Einscanh2 – hybrid led infrared light source handheld 3d scanner, 2025. Accessed: 2025-06-18.

[20] GoMeasure3D. Microscribe– affordable portable cmm, 2025. Accessed: 2025-06-18.

[21] Global Veterinary Surgery. Chapter 3 of the cutting edge is now live!, 2020. Accessed: 2025-06-18.

[22] BioRender.com. `https://BioRender.com`, 2025. Created with BioRender.com.

[23] Andriy Fedorov, Reinhard Beichel, Jayashree Kalpathy-Cramer, Julien Finet, Jean-Christophe Fillion-Robin, Sonia Pujol, Christian Bauer, Dominique Jennings, Fiona Fennessy, Milan Sonka, John Buatti, Stephen Aylward, James V. Miller, Steve Pieper, and Ron Kikinis. 3d slicer as an image computing platform for the quantitative imaging network. *Magnetic Resonance Imaging*, 30(9):1323–1341, 2012.

[24] Marnee J. McKay, Kenneth A. Weber, Evert O. Wesselink, Zachary A. Smith, Rebecca Abbott, David B. Anderson, Claire E. Ashton-James, John Atyeo, Aaron J. Beach, Joshua Burns, Stephen Clarke, Natalie J. Collins, Michel W. Coppieters, Jon Cornwall, Rebecca J. Crawford, Enrico De Martino, Adam G. Dunn, Jillian P. Eyles, Henry J. Feng, Maryse Fortin, Melinda M. Franettovich Smith, Graham Galloway, Ziba Gandomkar, Sarah Glastras, Luke A. Henderson, Julie A. Hides, Claire E. Hiller, Sarah N. Hilmer, Mark A. Hoggarth, Brian Kim, Navneet Lal, Laura LaPorta, John S. Magnussen, Sarah Maloney, Lyn March, Andrea G. Nackley, Shaun P. O'Leary, Anneli Peolsson, Zuzana Perraton, Annelies L. Pool-Goudzwaard, Margaret Schnitzler, Amee L. Seitz, Adam I. Semciw, Philip W. Sheard, Andrew C. Smith, Suzanne J. Snodgrass, Justin Sullivan, Vienna Tran, Stephanie Valentin, David M. Walton, Laurelie R. Wishart, and James M. Elliott. Musclemap: An open-source, community-supported consortium for whole-body quantitative mri of muscle. *Journal of Imaging*, 10(11):262, 2024.

[25] Jakob Wasserthal, Hanns-Christian Breit, Manfred T. Meyer, Maurice Pradella, Daniel Hinck, Alexander W. Sauter, Tobias Heye, Daniel T. Boll, Joshy Cyriac, Shan Yang, Michael Bach, and Martin Segeroth. Totalsegmentator: Robust segmentation of 104 anatomic structures in ct images. *Radiology: Artificial Intelligence*, 5(5), September 2023.

[26] Fabian Isensee, Jens Petersen, Andre Klein, David Zimmerer, Paul F. Jaeger, Simon Kohl, Jakob Wasserthal, Gregor Koehler, Tobias Norajitra, Sebastian Wirkert, and Klaus H. Maier-Hein. nnu-net: Self-adapting framework for u-net-based medical image segmentation, 2018.

[27] Qianqian Fang and David A. Boas. Tetrahedral mesh generation from volumetric binary and grayscale images. In *2009 IEEE International Symposium on Biomedical Imaging: From Nano to Macro*, pages 1142–1145, 2009.

[28] Robert McNeel & Associates. Rhinoceros 3d, 2023.

[29] Inge Söderkvist and Per-Åke Wedin. Determining the movements of the skeleton using well-configured markers. *Journal of Biomechanics*, 26(12):1473–1477, 1993.

[30] Samuel R. Ward and Richard L. Lieber. Density and hydration of fresh and fixed human skeletal muscle. *Journal of Biomechanics*, 38(11):2317–2320, 2005.

[31] Wilfrid Taylor Dempster. Rates of penetration of fixing fluids. *American Journal of Anatomy*, 107(1):59–72, 1960.

[32] A Cutts. Shrinkage of muscle fibres during the fixation of cadaveric tissue. *J Anat*, 160:75–78, 1988.

[33] J Mendez and A Keys. Density and composition of mammalian muscle. *Metabolism*, 9(2):184–188, 1960.

[34] Lachlan Bird, Arkiev D'Souza, Iain Ball, Caroline Rae, Robert D. Herbert, and Bart Bolsterlee. Validity and reliability of measurements of aponeurosis dimensions from magnetic resonance images. *Scandinavian Journal of Medicine amp; Science in Sports*, 29(6):808–815, 2019.

[35] Bart Bolsterlee. A new framework for analysis of three-dimensional shape and architecture of human skeletal muscles from in vivo imaging data. *Journal of Applied Physiology*, 132(3):712–725, 2022.

Appendix A. Tests 3D scanner

Appendix A.1. Foam phantom muscle

Rationale

A foam mock-up muscle was created as a preliminary and highly controlled model to test 3D scanning techniques prior to working with actual biological tissue. The intent was to familiarise with the scanning workflow, assess how marker points could be digitised, and investigate the impact of surface properties on scan registration. The shiny pink foam was chosen to mimic the reflective appearance of wet muscle tissue, while inserted nails served as physical reference points simulating fibre length measurements.

Materials and methods

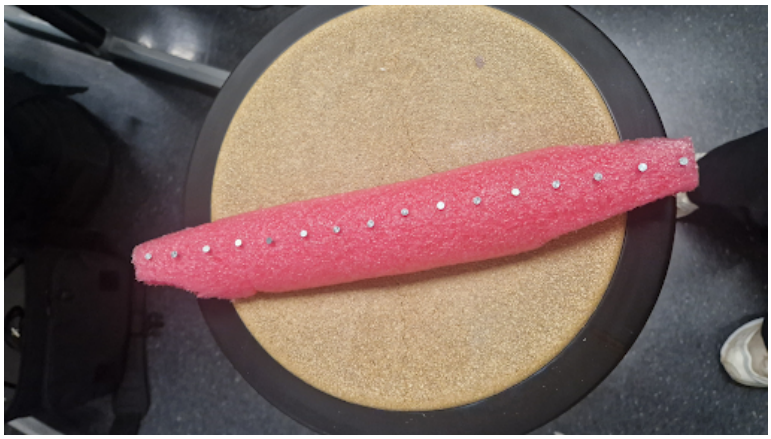

Figure A.5: Pink foam mock-up muscle attached to a skeleton. The shiny surface was intended to mimic the reflective effect of wet muscle tissue. Nails were inserted to simulate fibre length measurements.

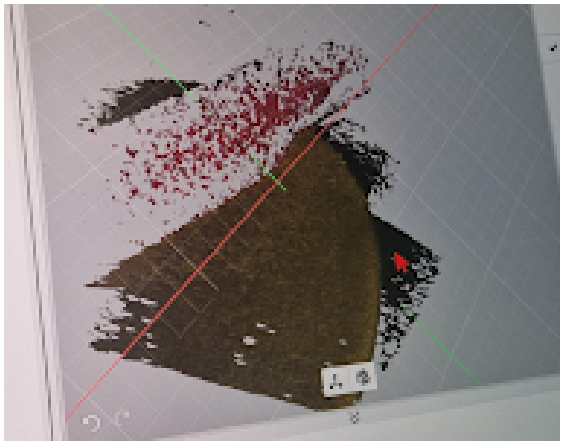

Figure A.6: 3D scan output of the foam mock-up muscle. The shiny surface caused registration issues, resulting in incomplete or distorted geometry.

The model was scanned using the available structured-light scanner at TU Delft. Both dry and wetted foam conditions were tested to compare against biological tissue. The scanning session aimed to evaluate how well the reflective surface would be captured and whether the nail markers could be clearly registered. Multiple scanning passes were attempted to improve registration.

Results

The reflective surface interfered strongly with the scanner's sensors, producing incomplete meshes and severe geometry distortion. Despite repeated passes, the registration failed to fill major surface gaps.

Both dry and wet foam conditions performed poorly, though their quality was broadly comparable to that of pig heart scans. Interestingly, metallic nails or pins were more reliably visible than the foam itself, suggesting that certain materials register better under the structured-light setup. The nail markers, however, remained only partially reconstructed and not suitable as reliable digitised landmarks.

Discussion and action points

The experiment revealed that:

- Surface reflectivity is a critical factor: shiny or wet surfaces lead to registration errors.
- Foam phantoms, whether dry or wet, show similar scanning difficulties as actual tissue.
- Small metallic markers (nails) are better detected than wet or porous materials but still incompletely captured.
- Even with careful operation, the scanner's ability to capture complete geometry on reflective materials was limited.

These findings prompted the following steps:

1. Conduct follow-up scans on actual muscle tissue to test performance on realistic biological surfaces.
2. Use two different 3D scanners to determine whether the limitations were hardware-specific.
3. Explore larger, matte-finished markers for improved detection.

Appendix A.2. Pig heart scans

Rationale

To validate the foam phantom results under realistic conditions, formaldehyde-fixed pig hearts were scanned. These specimens provided representative soft-tissue geometry and surface properties while remaining stable for extended handling.

Materials and methods

A professional operator at the Industrial Design faculty performed scans on five pig hearts over a two-hour period. The scanning involved multiple repositionings and rotations of the hearts to attempt full geometry capture. The effect of ambient light (dark vs. bright environment) was also tested.

Results

Scanning the pig hearts proved challenging. The following issues were observed:

- Large deformations occurred when rotating the hearts, complicating registration.
- Mesh quality remained low despite the operator's expertise, and full surface reconstruction was not achieved.
- Ambient lighting conditions (dark vs. bright) had negligible effect on scan quality.
- Based on the observed workflow, scanning a single pig leg might take as long as two hours.
- It remains uncertain whether all available scanners use the same technology or whether some hardware limitations are specific to the tested device.

Discussion and action points

The poor results on both foam and biological tissue indicate that structured-light scanning may not be well-suited for high-fidelity capture of wet or deformable anatomical specimens. The similarity between pig heart and foam results reinforces the relevance of the phantom model. Future work should include:

1. Benchmarking with a different scanning system to exclude hardware limitations.
2. Investigating fixation or coating methods to reduce deformation during handling.
3. Assessing whether more time-efficient workflows can be established, given that one leg may require several hours to scan.

Appendix A.3. Muscle phantom

Rationale

Building on the lessons from the foam phantom and pig heart scans, a muscle phantom from actual meat was prepared to replicate realistic dissection conditions. The specimen, a large piece of red meat with an embedded bone segment, was selected to mimic both the texture and internal complexity of dissected muscle. This follow-up aimed to:

- Assess whether anatomical landmark markers could be reliably detected in 3D scans.
- Practise scanning techniques on a specimen with realistic geometry, surface texture, and colour.
- Determine optimal marker type, size, and surface finish for subsequent anatomical dissections.

Materials and methods

Two types of markers were tested: shiny coloured plastic caps and plain white plastic caps. Marker placement was designed to replicate anatomical landmark positioning in a dissection setting. The meat was chosen to be big adn red (like actual muscles), and with a piece of bone to make the resemblance as clear as possible.

Results

Both marker types were successfully registered in the scans, but visual clarity varied. Larger and white markers produced cleaner registration and higher visibility in the final mesh. The 3D geometry was complete and accurate, with all markers correctly positioned. The surface texture, however, appeared glossy and somewhat artificial, resembling a high-quality render rather than a perfectly photorealistic texture.

Figure A.7: Muscle phantom in the shape of a large piece of meat with a bone segment

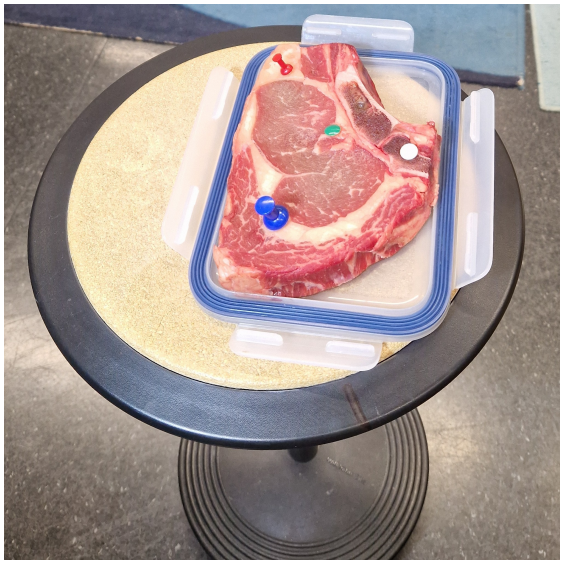

Figure A.8: Anatomical markers tested for visibility in 3D scans, including shiny coloured caps and white plastic caps.

Figure A.9: Final post-processed 3D scan of the specimen. The geometry is accurate and detailed, although the texture appears slightly glossy and artificial rather than fully photorealistic.

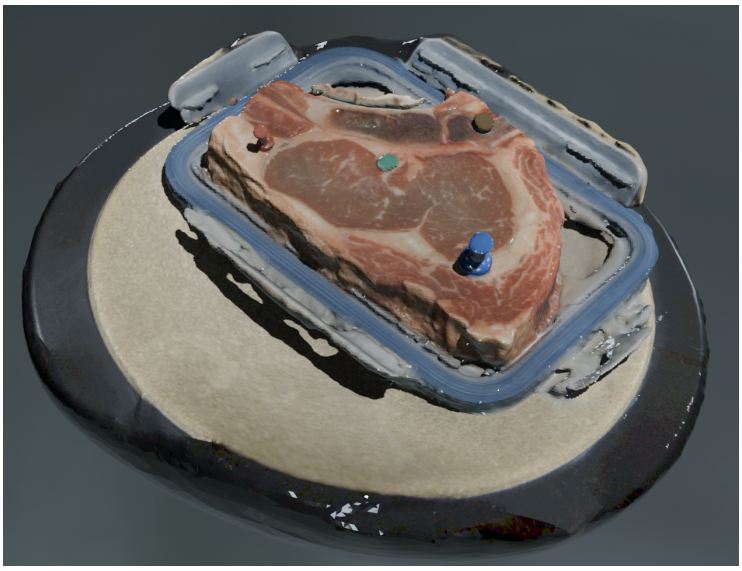

Figure A.10: Final scan with all anatomical markers (pins) in place. Larger and matte white markers provided the best visibility and scanning performance.

Discussion and action points

The experiment confirmed that:

- Marker size and surface finish are critical, large, matte white markers were optimal.
- Biological tissue with embedded bone can be effectively scanned if marker selection is optimised.
- Glossy surface appearance in the textures does not compromise geometric accuracy.

Based on these results, large matte light-colored wooden pins were selected for use in the pilot dissection. The study also demonstrated that with appropriate markers, high-quality 3D geometry can be obtained even on complex biological surfaces.

Appendix A.4. Photogrammetry test

Rationale

Following the muscle phantom experiment, a trial with photogrammetry was conducted to assess whether this technique could be incorporated into the dissection workflow to generate accurate 3D models of anatomical specimens. Photogrammetry was considered as a potential alternative to structured light scanning, with the advantage of requiring only a camera and dedicated reconstruction software.

Materials and methods

A cardboard box with a matte surface and sharp edges was used as a control object, as these features make it easy to reconstruct in 3D. A total of 120 high-resolution photographs were taken using a Canon DSLR camera, with consistent lighting and overlapping coverage from multiple angles. The images were processed in Meshroom to generate a textured 3D model.

A dedicated photogrammetry phone app could not be used because phones are prohibited in the dissection rooms due to privacy concerns due to the possibility of automatic backups to external servers.

Results

The reconstruction produced a model with accurate geometry and acceptable texture quality. The camera viewpoint reconstruction in Meshroom confirmed complete coverage of the object, and no major holes or distortions were visible in the final mesh.

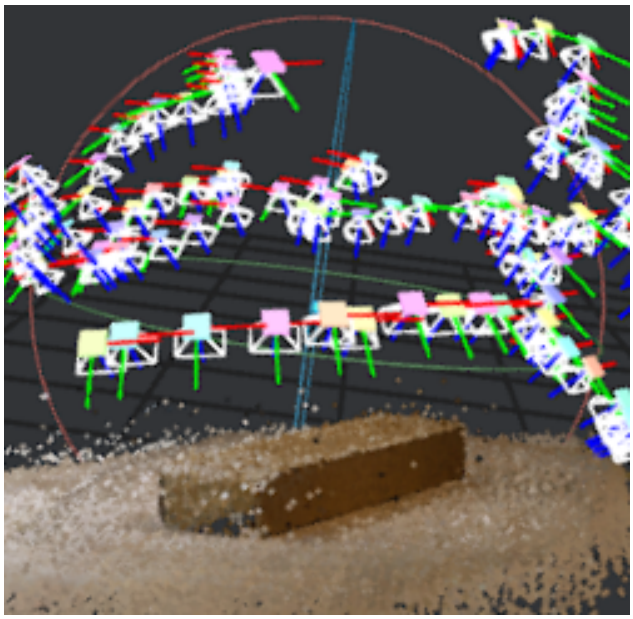

Figure A.11: 3D scan result of the cardboard box in photogrammetry software. The coloured boxes represent camera viewpoints defined during model reconstruction.

Discussion and action points

Despite the technical success of the reconstruction, the method was deemed unsuitable for live dissections:

- Processing a single set of 120 images required more than six hours, creating a significant bottleneck.
- Results could not be inspected immediately, making real-time quality control impossible.
- Rather than streamlining the workflow, the method would slow it down substantially during dissections.

Given these limitations, photogrammetry was not pursued further for anatomical scanning. Instead, efforts were focused on improving structured light scanning, building on the findings from the muscle phantom experiment, which offered faster turnaround and immediate quality verification.

Appendix B. Dissection pilot protocol

Preparation Protocol

Phase 1: Preparation of the Lower Limbs

1. Place the body in anatomical position, supine, on the table.
2. Identify and document relevant anatomical structures.
3. Remove skin to expose the muscle layers.
4. Test in the calcaneus which bone pin works best as a marker without damaging the structure:
   (a) concrete nail
   (b) nail
   (c) wooden capped pins
   (d) small screw
5. Pin bony landmarks using the chosen marker:
   (a) Anterior Superior Iliac Spine (ASIS)
   (b) Greater Trochanter
   (c) Lateral Femoral Condyle
   (d) Medial Femoral Condyle
6. Secure the hip and knee joints so they do not affect the scan and cannot move. If not possible, measure joint angles each time with a goniometer (target: $0, 0, 0°$).

Phase 2: MicroScribe & Artec Preparation

1. Connect the 3D MicroScribe™ digitizer to a laptop.
2. Determine the exact position using the floor/grid; optionally mark the position with marker pens.
3. Home the MicroScribe™ using the fixed-axes tool (metal tripod).
4. Launch Rhino and open the test file.
5. Measure distances between bone pins with the MicroScribe™; annotate and save them in the "Test" file. This establishes a coordinate system for registering bones and muscles.
6. Power on and warm up the Artec Spider and Artec Eva.
7. Calibrate both Artec scanners.
8. Perform a test scan to check whether the bone markers and tissue register correctly.

Protocol: Supine Position

Phase 3: Quadriceps

Preparation:

- Place the body in anatomical position, supine, on the table.

Muscle Group 1: Rectus Femoris & Sartorius

1. Pin the length of rectus femoris and sartorius in both legs and mark 10 fiber lengths per muscle.
2. Acquire multiple 3D scans of the leg.
3. Merge the 3D scans; enable scan mapping during subsequent measurements. Check intermittently that scans were successful.
4. Measure distances between pins with the MicroScribe™ arm:
   (a) bony landmarks
   (b) insertion points or curves
   (c) muscle length
   (d) 10 superficial muscle fiber lengths
5. Remove rectus femoris and sartorius.
6. Weigh rectus femoris and sartorius.

Muscle Group 2: Vastus Lateralis & Vastus Medialis

1. Pin the length of vastus lateralis and vastus medialis in both legs and mark 10 fiber lengths per muscle.
2. Acquire multiple 3D scans of the leg.

3. Merge the 3D scans; enable scan mapping during subsequent measurements. Check intermittently that scans were successful.
4. Measure distances between pins with the MicroScribe™ arm:
   (a) bony landmarks
   (b) insertion points or curves
   (c) muscle length
   (d) 10 superficial muscle fiber lengths
5. Remove vastus lateralis and vastus medialis.
6. Weigh vastus lateralis and vastus medialis.

Muscle Group 3: Vastus Intermedius

1. Pin the length of vastus intermedius in both legs and mark 10 fiber lengths per muscle.
2. Measure distances between pins with the MicroScribe™ arm:
   (a) bony landmarks
   (b) insertion points or curves
   (c) muscle length
   (d) 10 superficial muscle fiber lengths
3. Remove vastus intermedius.
4. Weigh vastus intermedius.

Protocol: Prone Position

Phase 4: Medial Adductors

Muscle Group 1: Adductor Longus, Gracilis, & Pectineus

1. Pin the length of adductor longus, gracilis, and pectineus; mark 10 fiber lengths per muscle.
2. Acquire multiple 3D scans of the leg.
3. Merge the 3D scans; enable scan mapping during subsequent measurements. Check intermittently that scans were successful.
4. Measure distances between pins with the MicroScribe™ arm:
   (a) bony landmarks
   (b) insertion points or curves
   (c) muscle length
   (d) 10 superficial muscle fiber lengths
5. Remove adductor longus, gracilis, and pectineus.
6. Weigh adductor longus, gracilis, and pectineus.

Muscle Group 2: Adductor Brevis & Adductor Magnus

1. Pin the length of adductor brevis and adductor magnus; mark 10 fiber lengths per muscle.
2. Acquire multiple 3D scans of the leg.
3. Merge the 3D scans; enable scan mapping during subsequent measurements. Check intermittently that scans were successful.
4. Measure distances between pins with the MicroScribe™ arm:
   (a) bony landmarks
   (b) insertion points or curves
   (c) muscle length
   (d) 10 superficial muscle fiber lengths
5. Remove adductor brevis and adductor magnus.
6. Weigh adductor brevis and adductor magnus.

Phase 5: Anterior Deep Hip Muscles

Muscle Group: Psoas & Iliacus

1. Pin the length of psoas and iliacus; mark 10 fiber lengths per muscle.
2. Acquire multiple 3D scans of the leg.
3. Merge the 3D scans; enable scan mapping during subsequent measurements. Check intermittently that scans were successful.
4. Measure distances between pins with the MicroScribe™ arm:
   (a) bony landmarks
   (b) insertion points or curves
   (c) muscle length

(d) 10 superficial muscle fiber lengths

5. Remove psoas and iliacus.
6. Weigh psoas and iliacus.

Phase 6: Gluteal & Lateral Deep Hip Muscles (Left)

Preparation:

- Place the body prone on the table (anterior side facing down).

Muscle Group 1: Gluteus Maximus

1. Pin the length of gluteus maximus; mark 10 fiber lengths in the muscle.
2. Acquire multiple 3D scans of the leg.
3. Merge the 3D scans; enable scan mapping during subsequent measurements. Check intermittently that scans were successful.
4. Measure distances between pins with the MicroScribe™ arm:
   (a) bony landmarks
   (b) insertion points or curves
   (c) muscle length
   (d) 10 superficial muscle fiber lengths
5. Remove gluteus maximus.
6. Weigh gluteus maximus.

Muscle Group 2: Gluteus Medius

1. Pin the length of gluteus medius; mark 10 fiber lengths in the muscle.
2. Acquire multiple 3D scans of the leg.
3. Merge the 3D scans; enable scan mapping during subsequent measurements. Check intermittently that scans were successful.
4. Measure distances between pins with the MicroScribe™ arm:
   (a) bony landmarks
   (b) insertion points or curves
   (c) muscle length
   (d) 10 superficial muscle fiber lengths
5. Remove gluteus medius.
6. Weigh gluteus medius.

Muscle Group 3: Gluteus Minimus & Tensor Fasciae Latae

1. Pin the length of gluteus minimus and tensor fasciae latae; mark 10 fiber lengths per muscle.
2. Acquire multiple 3D scans of the leg.
3. Merge the 3D scans; enable scan mapping during subsequent measurements. Check intermittently that scans were successful.
4. Measure distances between pins with the MicroScribe™ arm:
   (a) bony landmarks
   (b) insertion points or curves
   (c) muscle length
   (d) 10 superficial muscle fiber lengths
5. Remove gluteus minimus and tensor fasciae latae.
6. Weigh gluteus minimus and tensor fasciae latae.

Muscle Group 4: Deep Lateral Rotators

1. Pin the length of piriformis, obturator internus, obturator externus, gemellus superior, gemellus inferior, and quadratus femoris; mark 10 fiber lengths per muscle.
2. Acquire multiple 3D scans of the leg.
3. Merge the 3D scans; enable scan mapping during subsequent measurements. Check intermittently that scans were successful.
4. Measure distances between pins with the MicroScribe™ arm:
   (a) bony landmarks
   (b) insertion points or curves
   (c) muscle length
   (d) 10 superficial muscle fiber lengths
5. Remove these muscles one by one.
6. Weigh each muscle separately.

Phase 7: Gluteal & Deep Hip Muscles (Right)

Muscle Group 1: Gluteus Maximus

1. Pin the length of gluteus maximus; mark 10 fiber lengths in the muscle.
2. Acquire multiple 3D scans of the leg.
3. Merge the 3D scans; enable scan mapping during subsequent measurements. Check intermittently that scans were successful.
4. Measure distances between pins with the MicroScribe™ arm:
   (a) bony landmarks
   (b) insertion points or curves
   (c) muscle length
   (d) 10 superficial muscle fiber lengths
5. Remove gluteus maximus.
6. Weigh gluteus maximus.

Muscle Group 2: Gluteus Medius

1. Pin the length of gluteus medius; mark 10 fiber lengths in the muscle.
2. Acquire multiple 3D scans of the leg.
3. Merge the 3D scans; enable scan mapping during subsequent measurements. Check intermittently that scans were successful.
4. Measure distances between pins with the MicroScribe™ arm:
   (a) bony landmarks
   (b) insertion points or curves
   (c) muscle length
   (d) 10 superficial muscle fiber lengths
5. Remove gluteus medius.
6. Weigh gluteus medius.

Muscle Group 3: Gluteus Minimus & Tensor Fasciae Latae

1. Pin the length of gluteus minimus and tensor fasciae latae; mark 10 fiber lengths per muscle.
2. Acquire multiple 3D scans of the leg.
3. Merge the 3D scans; enable scan mapping during subsequent measurements. Check intermittently that scans were successful.
4. Measure distances between pins with the MicroScribe™ arm:
   (a) bony landmarks
   (b) insertion points or curves
   (c) muscle length
   (d) 10 superficial muscle fiber lengths
5. Remove gluteus minimus and tensor fasciae latae.
6. Weigh gluteus minimus and tensor fasciae latae.

Muscle Group 4: Deep Lateral Rotators

1. Pin the length of piriformis, obturator internus, obturator externus, gemellus superior, gemellus inferior, and quadratus femoris; mark 10 fiber lengths per muscle.
2. Acquire multiple 3D scans of the leg.
3. Merge the 3D scans; enable scan mapping during subsequent measurements. Check intermittently that scans were successful.
4. Measure distances between pins with the MicroScribe™ arm:
   (a) bony landmarks
   (b) insertion points or curves
   (c) muscle length
   (d) 10 superficial muscle fiber lengths
5. Remove these muscles one by one.
6. Weigh each muscle separately.

Phase 8: Hamstrings

Muscle Group 1: Biceps Femoris (long head) & Semitendinosus

1. Pin the length of biceps femoris (long head) and semitendinosus; mark 10 fiber lengths per muscle.
2. Acquire multiple 3D scans of the leg.
3. Merge the 3D scans; enable scan mapping during subsequent measurements. Check intermittently that scans were successful.

4. Measure distances between pins with the MicroScribe™ arm:
   (a) bony landmarks
   (b) insertion points or curves
   (c) muscle length
   (d) 10 superficial muscle fiber lengths
5. Remove biceps femoris (long head) and semitendinosus.
6. Weigh biceps femoris (long head) and semitendinosus.

Muscle Group 2: Biceps Femoris (short head) & Semimembranosus

1. Pin the length of biceps femoris (short head) and semimembranosus; mark 10 fiber lengths per muscle.
2. Acquire multiple 3D scans of the leg.
3. Merge the 3D scans; enable scan mapping during subsequent measurements. Check intermittently that scans were successful.
4. Measure distances between pins with the MicroScribe™ arm:
   (a) bony landmarks
   (b) insertion points or curves
   (c) muscle length
   (d) 10 superficial muscle fiber lengths
5. Remove biceps femoris (short head) and semimembranosus.
6. Weigh biceps femoris (short head) and semimembranosus.

Appendix C. Dissection pilot results

Rationale

The aim of this pilot was to test the full dissection protocol on a fresh donor leg to assess feasibility, optimize workflow, and identify necessary adjustments before the main study. This included testing the integration of 3D scanning and Microscribe measurements, and evaluating the visibility of anatomical markers and muscles.

Figure C.12 shows the initial concept of the complete experimental pipeline for the final dissection, including both a fresh and an embalmed body.

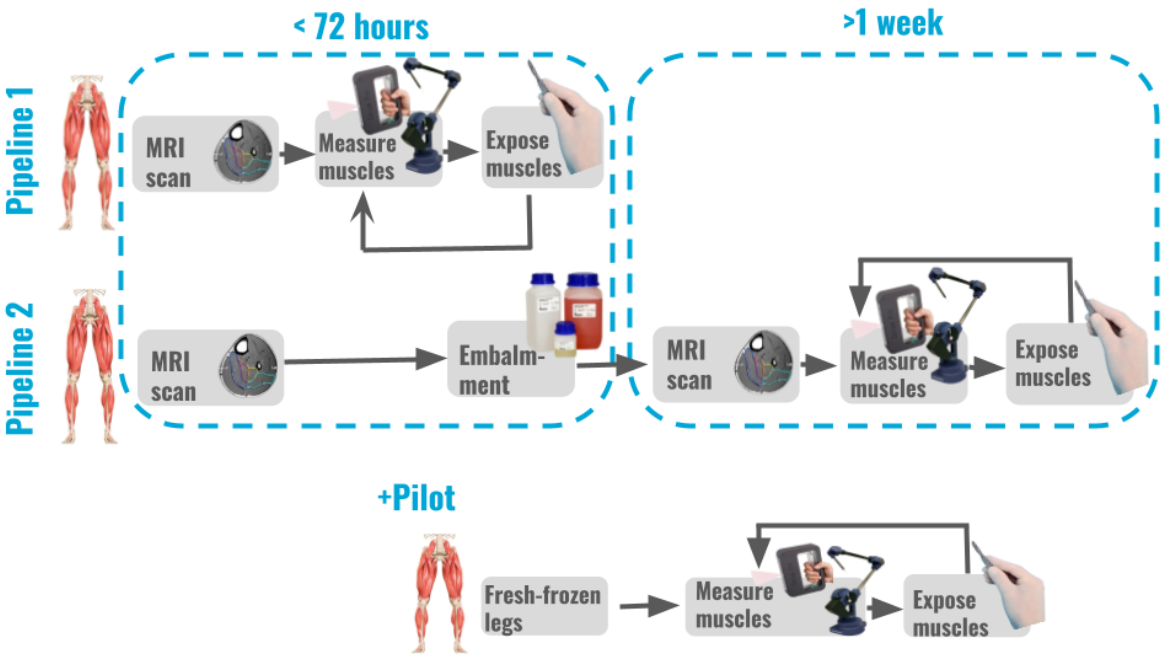

Figure C.12: Initial concept of the full experimental pipeline for the final dissection using both a fresh and an embalmed body.

The 3D scan were aligned in the Artec studio software, and afterwars rednered in Blender for good visualisation of the scans output.

Materials

- One fresh (non-embalmed) human donor leg from a female, 82 years old, defrosted for three days.
- Dissection instruments (scalpels, scissors, forceps, gloves, gowns, etc.).
- Microscribe GX™ digitizer.
- Artec Eva and Spider 3D scanners.
- Anatomical markers.
- Photography equipment (dissection room camera).

Results

Three muscles were fully dissected, weighed, and scanned during the pilot (Table C.6). The measured weights reflect the relatively high fat content present in some muscles, particularly the gluteus maximus. While fat was not removed prior to weighing, the images from the scans show the overall muscle outline and texture well enough for preliminary evaluation.

The scans (Figure C.13) show the entire leg within the frame, with photorealistic surface rendering: a feature that is essential for accurate landmark registration. Although some muscle fibers are faintly visible, the surface appears somewhat shiny, consistent with the wet condition of the tissue. In the gluteus maximus, a lot of decay of the muscle can be seen through the blotchy (not smooth) structure of its surface.

Muscle	Weight (g)
Rectus femoris	74
Sartorius	53
Gluteus maximus	378

Table C.6: Measured weights of dissected muscles during the pilot study.

Gluteus maximus (posterior) **Rectus femoris** (anterior) **Sartorius** (anterior)

Figure C.13: Three 3D scans from the dissection pilot: gluteus maximus, rectus femoris, and sartorius.

Points noticed during the pilot.

- **Time constraints:** Planned to process both legs and 20 muscles; in practice only 3 muscles on one leg were completed within 3 hours.
- **Deskinning duration:** Skin removal alone took ~3 hours (about 1.5 hours longer than expected), leaving insufficient time for excision and measurement.
- **Specimen characteristics:** Female donor with very small muscles, reducing initial visibility and making separation more difficult.
- **Prior use and decomposition:** The specimen had been used before and was partly uncovered for a period, so despite being fresh (non-embalmed) it showed advanced decomposition.
- **Gluteus maximus:** No distinct fibers visible due to decay; did not come off in one piece; substantial adherent fat complicated clean dissection.
- **Marker stability:** Markers were visible in scans but showed slight wobble/mobility.
- **Muscle texture/handling:** Muscles appeared loose/sloppy; a fresh leg in this condition is not preferred for the protocol.

- **3D scanning limits (deep rotators):** Deep lateral rotator muscles are likely too small and too occluded to be captured: the scanner only reconstructs the exposed top surface, and these muscles lie between pelvis and femur, so their superior surface is not visible with bone in front of it.
- **Fat on muscles:** A lot of fat was still attached to the excised muscles, which may have affected weight measurements; density assessment is necessary in future dissections.

Action points for the main dissection

1. **Add density assessment:** Measure volume and mass to derive density and account for variable fat content (not measured in the pilot).
2. **Exclude deep hip muscles:** Do not attempt surface scanning of deep lateral rotators due to occlusion and size.
3. **Extend schedule:** Plan a minimum of 3 days (not 1) to complete the full protocol.
4. **Use only the fixated specimen pipeline:** Proceed with the fixated workflow (omit the fresh pathway for this study).
5. **Stabilize markers:** Evaluate screwing markers directly into bony landmarks to eliminate wobble.
6. **Specimen strategy:** Future feasibility testing should prioritize male donors to optimize visibility during dissection. While this approach might seem counterproductive, since the pipeline should ultimately work with both male and female donors, this strategy is recommended for practical reasons, given the exploratory nature of this research. Since the study is investigating whether 3D scanning can serve as a viable validation technique and requires dissection by a relatively inexperienced researcher, the typically lower fat-to-muscle ratio and more prominent muscle definition in male specimens would facilitate muscle identification and make the dissection process more manageable.

Appendix D. Einscan H1 scanner test

Rationale

Following the dissection pilot and earlier 3D scanning tests with the Artec EVA and Spider scanners, a newer scanner model was sought to improve scan quality and speed. Through the hospital's plastic surgery department, we were able to test an Einscan H1 together with a high-performance laptop. This allowed evaluation of both the scanner's performance on anatomical tissue and the influence of background materials on scan quality.

Method

A cadaver arm was scanned in both skinned and deskinned/prepared condition. During the dissection pilot, reflections from the stainless steel dissection table caused noticeable artifacts in the 3D scans. To prevent this, the arm was placed on surgical drapes during the Einscan H1 test, using both a white and a blue drape for comparison. No significant difference in scan quality was found between the two drape colors, but both effectively reduced reflections compared to scanning directly on the table.

The hospital's medical photographer accompanied us during this pilot to assist with handling the new scanning technology and to ensure correct and authorised use of the equipment.

The 3D scan renders presented in this appendix were created in Blender.

Results

- The Einscan H1 produced detailed and complete scans of both the skinned and deskinned arm.
- The matte skin surface was particularly well captured, but the muscle tissue also registered clearly.
- Using a drape improved scan quality by preventing reflection artifacts caused by the table surface.
- Compared to the Artec EVA and Spider, the Einscan H1 provided faster acquisition with better detail, suggesting that the older TU Delft scanners (10 years old) may be limiting scan quality in previous trials.

Figure D.14: Full render from the Einscan H1 pilot showing a skinned and deskinned cadaver arm. Both surfaces were captured with high detail.

Figure D.15: Close-up photograph of the prepped arm, showing the exposed muscle surfaces.

Figure D.16: Einscan H1 test on a cadaver arm. Using a surgical drape prevented reflection artifacts caused by the stainless steel dissection table. The pilot was conducted with the assistance of the hospital's medical photographer.

Conclusion

The Einscan H1 pilot demonstrated substantially improved scan quality and acquisition speed compared to the older TU Delft Artec scanners. Given the clear advantages in anatomical detail, reduced artifact risk, and operational efficiency, the department's Innovation Lab decided to invest in an Einscan scanner together with a high-performance laptop to support future dissection and anatomical documentation work.

Appendix E. Volume measurement accuracy test

Rationale

Before applying water displacement to measure muscle volumes, the accuracy of two measurement methods was tested using a 3D-printed cube (Fig. E.18) of known volume.

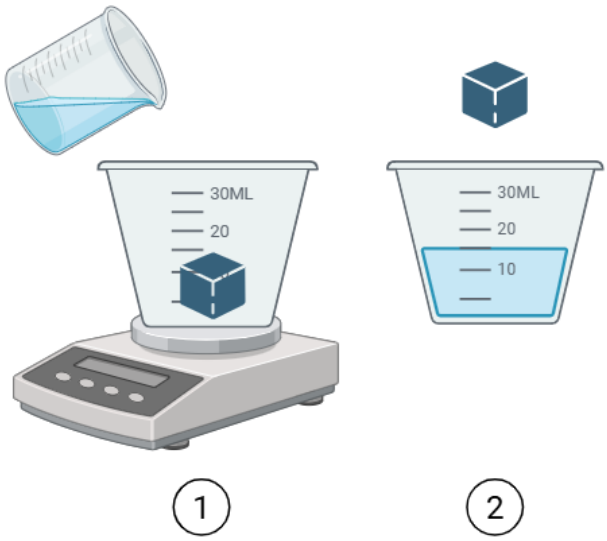

Figure E.17: Graphic representation of the two volume measurements that were tested for accuracy.

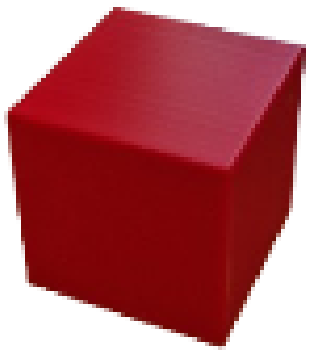

Figure E.18: 3D-printed test cube ($4 \cdot 4 \cdot 4$ cm, 64 mL).

Materials

- 3D-printed cube (dimensions: $4 \cdot 4 \cdot 4$ cm, volume 64 cm^3 or 64 mL)
- Measuring cup with 1 L scale
- Water
- Digital scale (accuracy: 1 g)

Methods

Two approaches were tested (Fig. E.17), each repeated three times:

1. **Filling method:** Place the cube in the measuring cup and add water until the 1 L mark is reached. Weigh the total water added and convert to volume (100 g = 100 mL).
2. **Submersion method:** Place the cube in a partially filled measuring cup and visually read the increase in water level.

Results

Table E.7: Volume measurements for both methods. Known cube volume: 64 mL.

Trial	Filling method (mL)	Submersion method (mL)
1	63	70
2	64	58
3	63	72
Mean error	~1 mL	~6 mL

Conclusion

The filling method (method 1) was more accurate, with an average deviation of approximately 1 mL, compared to ~6 mL for the submersion method. The filling method will therefore be used in the main dissection study to obtain muscle volume measurements.

Appendix F. FFP paint test

Figure F.19: Correctly painted veins and arteries, following anatomical color conventions (red for arteries, blue for veins).

Figure F.20: Anatomical window during muscle dissection without paint. Natural muscle fibers and surrounding tissue visible.

Figure F.21: Same anatomical window with painted arteries and veins. Paint leakage outside muscle borders is visible.

The paint was originally intended to highlight muscle borders in 3D scans, allowing clearer separation of structures during digital segmentation. However, during application on dissected muscles:

- The surface texture of the muscle was irregular and moist, reducing paint adhesion.
- Paint drizzled and spread beyond the muscle margins, obscuring the true anatomical boundaries.
- As a result, sharp outlines could not be guaranteed in the resulting 3D reconstructions.

For these reasons, unpainted dissections were used for the scanning process to preserve accurate geometry and structural clarity.

Appendix G. MRI scan settings

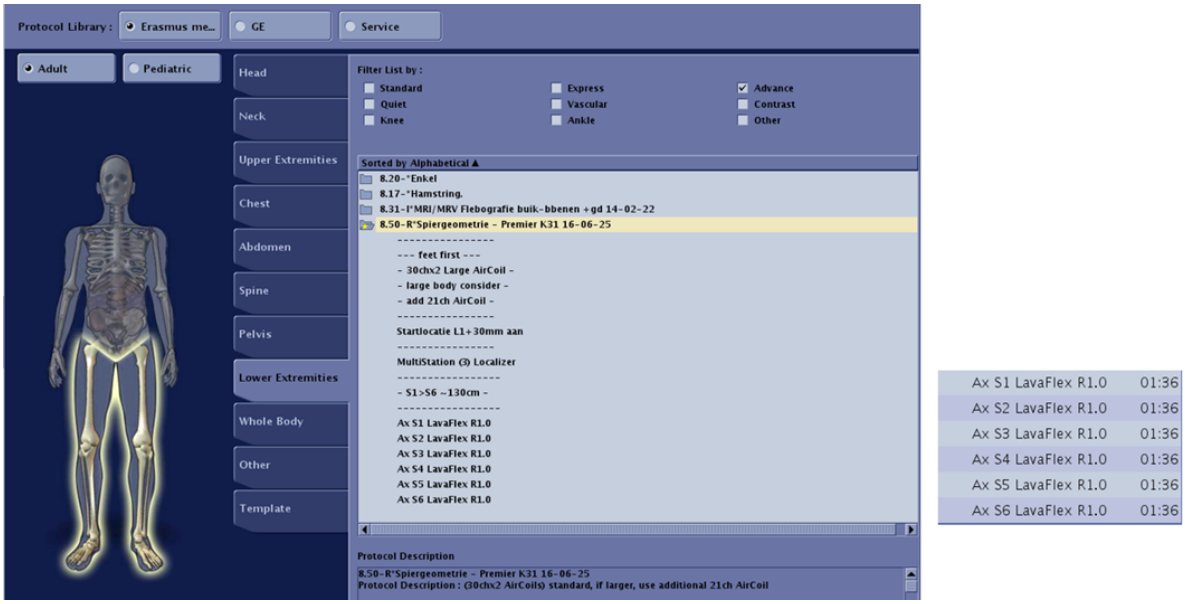

Figure G.22: MRI protocol library selection screen (GE software). The highlighted protocol includes scanning from feet first using a 30ch×2 Large AirCoil, starting location at L1+30 mm, and MultiStation Localizer imaging S1–S6 with LavaFlex R1.0 sequences.

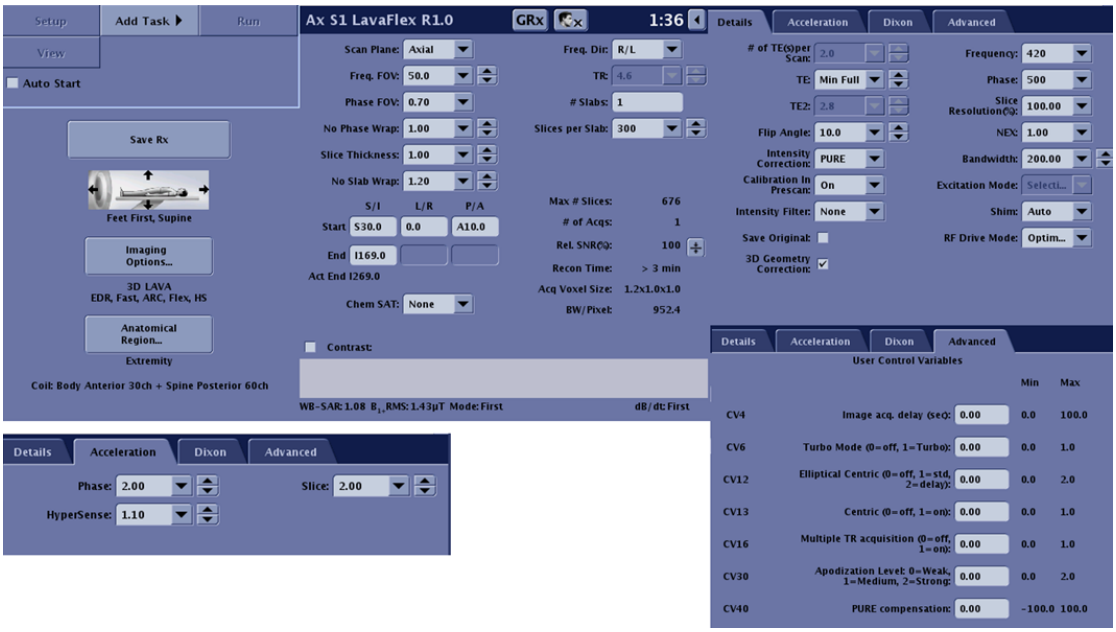

Figure G.23: Detailed scan parameter setup for the Ax S1 LavaFlex R1.0 sequence

Notes

- Femoral head oil capsule placement was inconsistent and therefore disregarded in the analysis.
- Oil capsules positioned at the SIPS broke in the supine position and were therefore not visible in the scans.

Appendix H. Main dissection protocol

Protocol: preparation

Phase 0: bony landmarks

1. Place the fixed body on the dissection table.
2. Pre-drill bony structures and mark them with a white-capped pushpin at the locations of the oil-bead markers:
   (a) Posterior superior iliac spine (PSIS)
   (b) Anterior superior iliac spine (ASIS)
   (c) Lateral femoral condyle
   (d) Medial femoral condyle
   (e) Medial tibial condyle

Phase 1: MicroScribe preparation

1. Connect the MicroScribe GX™ 3D spatial digitizer to a laptop and calibrate it.
2. Set up separate layers per muscle; verify that point-cloud assignment is on the correct *layer*.
3. Check that the MicroScribe base on the table does not wobble. Ensure it "moves with" the body (i.e., mount it to the same table as the body).
4. Wrap a small piece of cling film around the MicroScribe tip to keep it clean.

Phase 2: 3D scanner calibration

1. Connect the Artec Spider handheld 3D scanner to the laptop and power; allow ~20 minutes to warm up to room conditions.
2. Calibrate the Artec Spider according to the on-screen instructions.
3. Perform a test scan of the table to check for reflections. If reflections are excessive, hang surgical drapes.

Phase 3: preparation of the lower extremities

1. Position the body supine (anatomical position) on the table.
2. Identify and document relevant anatomical structures.
3. Remove skin and fat to expose the muscle layers.
4. Cover screws placed in bone with a matte white cap (well detected by the handheld 3D scanner).
5. Measure distances between bone pins with the MicroScribe™ into a test file.
6. Test the capped screws with the handheld 3D scanner.

Protocol: supine position

Phase 4: quadriceps

Preparation:

- Position the body supine (anatomical position) on the table.

Muscle group 1: rectus femoris, sartorius, and tensor fasciae latae

1. Pin overall muscle length for rectus femoris, sartorius, and tensor fasciae latae on both legs, and place 10 fibre-length pins per muscle.
2. Acquire multiple handheld 3D scans of the leg.
3. Merge the scans; keep scan mapping enabled during subsequent measurements. Intermittently verify scan success.
4. Measure distances between pins with the MicroScribe™ arm:
   (a) Bony landmarks
   (b) Insertion points or curves
   (c) Muscle length
   (d) Ten superficial muscle fibre lengths
5. Excise rectus femoris, sartorius, and tensor fasciae latae.
6. Weigh rectus femoris, sartorius, and tensor fasciae latae in an empty measuring cup.
7. Measure muscle volume by adding water to the measuring cup up to the 1 L mark.
8. Document all measurements in the Excel form.

Muscle group 2: vastus lateralis & vastus medialis

1. Pin muscle length for vastus lateralis and vastus medialis on both legs, and place 10 fibre-length pins per muscle.
2. Acquire multiple handheld 3D scans of the leg.
3. Merge the scans; keep scan mapping enabled during subsequent measurements. Intermittently verify scan success.
4. Measure distances between pins with the MicroScribe™ arm:
   (a) Bony landmarks
   (b) Insertion points or curves
   (c) Muscle length
   (d) Ten superficial muscle fibre lengths
5. Excise vastus lateralis and vastus medialis.
6. Weigh vastus lateralis and vastus medialis.
7. Measure muscle volume by adding water to the measuring cup up to the 1 L mark.
8. Document all measurements in the Excel form.

Muscle group 3: vastus intermedius

1. Pin muscle length for vastus intermedius on both legs, and place 10 fibre-length pins in the muscle.
2. Measure distances between pins with the MicroScribe™ arm:
   (a) Bony landmarks
   (b) Insertion points or curves
   (c) Muscle length
   (d) Ten superficial muscle fibre lengths
3. Excise vastus intermedius.
4. Weigh vastus intermedius.
5. Measure muscle volume by adding water to the measuring cup up to the 1 L mark.
6. Document all measurements in the Excel form.

Phase 5: medial adductors

Muscle group 1: adductor longus, gracilis, and pectineus

1. Pin muscle length for adductor longus, gracilis, and pectineus, and place 10 fibre-length pins per muscle.
2. Acquire multiple handheld 3D scans of the leg.
3. Merge the scans; keep scan mapping enabled during subsequent measurements. Intermittently verify scan success.
4. Measure distances between pins with the MicroScribe™ arm:
   (a) Bony landmarks
   (b) Insertion points or curves
   (c) Muscle length
   (d) Ten superficial muscle fibre lengths
5. Excise adductor longus, gracilis, and pectineus.
6. Weigh adductor longus, gracilis, and pectineus.
7. Measure muscle volume by adding water to the measuring cup up to the 1 L mark.
8. Document all measurements in the Excel form.

Muscle group 2: adductor brevis and adductor magnus

1. Pin muscle length for adductor brevis and adductor magnus, and place 10 fibre-length pins per muscle.
2. Acquire multiple handheld 3D scans of the leg.
3. Merge the scans; keep scan mapping enabled during subsequent measurements. Intermittently verify scan success.
4. Measure distances between pins with the MicroScribe™ arm:
   (a) Bony landmarks
   (b) Insertion points or curves
   (c) Muscle length
   (d) Ten superficial muscle fibre lengths
5. Excise adductor brevis and adductor magnus.
6. Weigh adductor brevis and adductor magnus.
7. Measure muscle volume by adding water to the measuring cup up to the 1 L mark.

8. Document all measurements in the Excel form.

Phase 6: anterior deep hip muscles

Muscle group: psoas major and iliacus

1. Pin muscle length for psoas and iliacus, and place 10 fibre-length pins per muscle.
2. Acquire multiple handheld 3D scans of the leg.
3. Merge the scans; keep scan mapping enabled during subsequent measurements. Intermittently verify scan success.
4. Measure distances between pins with the MicroScribe™ arm:
   (a) Bony landmarks
   (b) Insertion points or curves
   (c) Muscle length
   (d) Ten superficial muscle fibre lengths
5. Excise psoas and iliacus.
6. Weigh psoas and iliacus.
7. Measure muscle volume by adding water to the measuring cup up to the 1 L mark.
8. Document all measurements in the Excel form.

Protocol: prone position

Phase 7: gluteal and lateral deep hip muscles

Preparation:

- Turn the body prone (anterior side down) on the table.

Muscle group 1: gluteus maximus

1. Pin overall muscle length for gluteus maximus and place 10 fibre-length pins in the muscle.
2. Acquire multiple handheld 3D scans of the leg.
3. Merge the scans; keep scan mapping enabled during subsequent measurements. Intermittently verify scan success.
4. Measure distances between pins with the MicroScribe™ arm:
   (a) Bony landmarks
   (b) Insertion points or curves
   (c) Muscle length
   (d) Ten superficial muscle fibre lengths
5. Excise gluteus maximus.
6. Weigh gluteus maximus.
7. Measure muscle volume by adding water to the measuring cup up to the 1 L mark.
8. Document all measurements in the Excel form.

Muscle group 2: gluteus medius

1. Pin overall muscle length for gluteus medius and place 10 fibre-length pins in the muscle.
2. Acquire multiple handheld 3D scans of the leg.
3. Merge the scans; keep scan mapping enabled during subsequent measurements. Intermittently verify scan success.
4. Measure distances between pins with the MicroScribe™ arm:
   (a) Bony landmarks
   (b) Insertion points or curves
   (c) Muscle length
   (d) Ten superficial muscle fibre lengths
5. Excise gluteus medius.
6. Weigh gluteus medius.
7. Measure muscle volume by adding water to the measuring cup up to the 1 L mark.
8. Document all measurements in the Excel form.

Muscle group 3: gluteus minimus

1. Pin overall muscle length for gluteus minimus and place 10 fibre-length pins in the muscle.

2. Acquire multiple handheld 3D scans of the leg.
3. Merge the scans; keep scan mapping enabled during subsequent measurements. Intermittently verify scan success.
4. Measure distances between pins with the MicroScribe™ arm:
   (a) Bony landmarks
   (b) Insertion points or curves
   (c) Muscle length
   (d) Ten superficial muscle fibre lengths
5. Excise gluteus minimus.
6. Weigh gluteus minimus.
7. Measure muscle volume by adding water to the measuring cup up to the 1 L mark.
8. Document all measurements in the Excel form.

Phase 8: hamstrings

Muscle group 1: biceps femoris (long head) and semitendinosus

1. Pin muscle length for biceps femoris (long head) and semitendinosus, and place 10 fibre-length pins per muscle.
2. Acquire multiple handheld 3D scans of the leg.
3. Merge the scans; keep scan mapping enabled during subsequent measurements. Intermittently verify scan success.
4. Measure distances between pins with the MicroScribe™ arm:
   (a) Bony landmarks
   (b) Insertion points or curves
   (c) Muscle length
   (d) Ten superficial muscle fibre lengths
5. Excise biceps femoris (long head) and semitendinosus.
6. Weigh biceps femoris (long head) and semitendinosus.
7. Measure muscle volume by adding water to the measuring cup up to the 1 L mark.
8. Document all measurements in the Excel form.

Muscle group 2: biceps femoris (short head) and semimembranosus

1. Pin muscle length for biceps femoris (short head) and semimembranosus, and place 10 fibre-length pins per muscle.
2. Acquire multiple handheld 3D scans of the leg.
3. Merge the scans; keep scan mapping enabled during subsequent measurements. Intermittently verify scan success.
4. Measure distances between pins with the MicroScribe™ arm:
   (a) Bony landmarks
   (b) Insertion points or curves
   (c) Muscle length
   (d) Ten superficial muscle fibre lengths
5. Excise biceps femoris (short head) and semimembranosus.
6. Weigh biceps femoris (short head) and semimembranosus.
7. Measure muscle volume by adding water to the measuring cup up to the 1 L mark.
8. Document all measurements in the Excel form.

Appendix I. Definition origin and insertion of the studied muscles in this research scope

This table presents the anatomical origin and insertion points for 20 major thigh muscles using three definition approaches. The Anatomical columns provide standard anatomical descriptions based on classical terminology and bony landmarks from anatomical textbooks. However, these definitions sometimes differ from measured origins and insertions when textbook definitions could not be directly measured during dissection. For example, the vastus intermedius origin is described as the ”upper two-thirds of anterior and lateral surfaces of femur,” but this site cannot be measured with the MicroScribe arm when the muscle remains attached, requiring modified definitions. The measured columns accommodate definitions based on muscle attachment site identification in derived from MicroScribe digitization measurements during dissection. The modeled section explains how these different insertion and origin definitions were digitally defines: as a polyline or point.

Muscle	Anatomical		Measured		Modelled	
	Origin	**Insertion**	**Origin**	**Insertion**	**Origin**	**Insertion**
RF	Anterior inferior iliac spine and groove above acetabulum	Base of patella and tibial tuberosity via patellar ligament	The entire patellar ligament surround patella	-	Line	Line
SAR	Anterior superior iliac spine	Upper part of medial surface of tibia	-	-	Point	Point
TFL	Anterior part of outer lip of iliac crest	Iliotibial tract	-	-	Line	Line
VL	Greater trochanter, intertrochanteric line, linea aspera	Lateral border of patella and tibial tuberosity	-	-	Line	Line
VM	Intertrochanteric line, medial lip of linea aspera	Medial border of patella and tibial tuberosity	-	-	Line	Line
VI	Upper two-thirds of anterior and lateral surfaces of femur	Deep surface of quadriceps tendon and lateral border of patella	Most proximal anterior and lateral surfaces of femur that the intermedius is present	-	Line	Line
AL	Body of pubis below pubic crest	Middle third of medial lip of linea aspera	-	-	Multiple lines	Line
GRA	Body and inferior ramus of pubis	Upper part of medial surface of tibia	-	-	Line	Line
PEC	Superior ramus of pubis	Pectineal line of femur	-	-	Line	Line
AB	Inferior ramus of pubis and ramus of ischium	Lower third of medial lip of linea aspera	-	-	Point	Multiple points
AM	Inferior ramus of pubis and ramus of ischium	Linea aspera and medial supracondylar line	-	-	Line	Multiple lines
PM	Bodies and transverse processes of T12-L5 vertebrae	Lesser trochanter of femur	The process of the L5 vertebrae	-	Line	Line
IL	Iliac fossa and anterior sacroiliac ligaments	Lesser trochanter of femur	-	-	Line	Line
GMax	Ilium posterior to posterior gluteal line, sacrum, coccyx	Iliotibial tract and gluteal tuberosity of femur	Posterior ilium, sacrum and coccyx	Iliotibial tract	Line	Line
GMed	External surface of ilium between anterior and posterior gluteal lines	Lateral surface of greater trochanter	proximal posterior glutal line of ilium	-	Line	Line
GMin	External surface of ilium between anterior and inferior gluteal lines	Anterior border of greater trochanter	inferior posterior glutal line	-	Line	Line
BFlh	Ischial tuberosity	Head of fibula and lateral condyle of tibia	-	-	Point	Point
ST	Ischial tuberosity	Medial surface of upper part of tibia	-	-	Point	Multiple points
BFsh	Lateral lip of linea aspera, lateral supracondylar line	Head of fibula and lateral condyle of tibia	-	-	Line	Line
SM	Ischial tuberosity	Posterior part of medial condyle of tibia	-	-	Line	Point

Appendix J. Automatic segmentation toolboxes

Three different approaches were tested for automatic segmentation of lower leg muscles in mDixon MRI images:

- **QMRI**: A Mathematica toolbox that was used on the out-of-phase mDixon data. This method was unable to produce usable segmentation results for the dataset and was therefore excluded from further analysis.
- **TotalSegmentator**: A 3D slicer toolbox, which did not include all specified lower leg muscles in its segmentation output, but segmented the bones accurately.
- **MuscleMap**: A 3D slicer toolbox, which performed well at segmenting individual muscles with good anatomical detail. However, it did not reliably capture all relevant structures outside its predefined muscle set.

Given the complementary strengths of MuscleMap and TotalSegmentator, the outputs of these two methods were combined as a starting point of the segmentation process:

- Individual muscles were taken from **MuscleMap**.
- Bone structures were taken from **TotalSegmentator**.

Manual segmentation complemented the automatic segmentation.

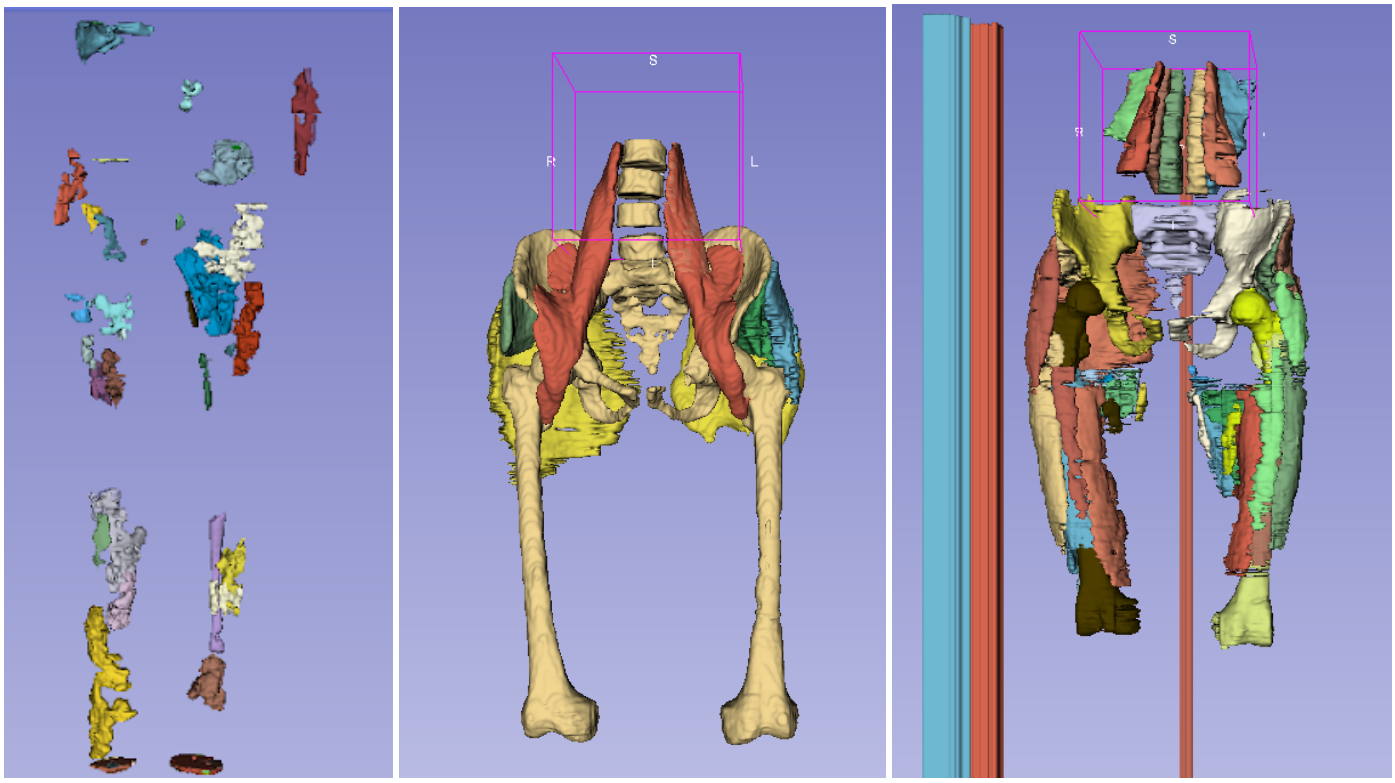

QMRI: Failed to produce usable lower leg muscle segmentation.

TotalSegmentator: Accurate for some muscles and bones, but missing most of the required muscles.

MuscleMap: Good anatomical detail for individual muscles, but incomplete overall coverage. Some of the muscle segmentations generated large cylinders in the far corner of the MRI image. These were deleted.

Figure J.24: Comparison of segmentation results from the three tested toolboxes.

Appendix K. Time breakdown experimental pipeline

Table K.9: Breakdown of tasks, hours, persons involved, and calculated person-hours during the data acquisition of the pipeline

Method	Hours	Persons	person-hours
MRI			
MRI 1	1.50	1	1.50
MRI 2	1.50	1	1.50
Segmentation automatic	2.00	1	2.00
Segmentation muscles MR1 supine	56.00	1	56.00
Segmentation muscles MR2 prone	24.00	1	24.00
Segmentation muscles MR2 supine	24.00	1	24.00
Segmentation markers MR2	1.00	1	1.00
Segmentation aponeuroses MR2	10.00	1	10.00
Dissection Preparation			
Setting up	1.00	1	1.00
Exposing first layer	5.00	4	20.00
Prone: Gmax, ST, BfLh			
3D scans	0.25	1	0.25
Microscribe	1.50	2	3.00
Remove and measure muscle	1.25	4	5.00
Remove fascia and fat new layer	0.25	4	1.00
Prone: Gmed, SM, BfSh			
3D scans	0.25	1	0.25
Microscribe	1.50	2	3.00
Remove and measure muscle	1.00	2	2.00
Remove fascia and fat new layer	0.50	2	1.00
Prone: Gmin			
3D scans	0.50	1	0.50
Microscribe	0.50	2	1.00
Remove and measure muscle	1.00	2	2.00
Supine: RF, SAR, TFL			
Turn body and place bone marks	0.50	2	1.00
3D scans	0.50	1	0.50
Microscribe	1.00	2	2.00
Remove and measure muscle	2.00	2	4.00
Remove fascia and fat new layer	0.50	2	1.00
Supine: VL, VM			
3D scans	0.50	1	0.50
Microscribe	1.00	1	1.00
Remove and measure muscle	2.00	2	4.00
Remove fascia and fat new layer	0.50	2	1.00
Supine: Vin			
3D scans	0.50	1	0.50
Microscribe	0.50	1	0.50
Remove and measure muscle	2.00	2	4.00
Remove fascia and fat new layer	0.50	2	1.00
Supine: AL, AB, GRA, PEC			
3D scans	0.50	1	0.50
Microscribe	1.00	2	2.00
Remove and measure muscle	1.00	2	2.00
Supine: PM, IL, AM			
Open belly and put intestines aside	1.50	2	3.00
3D scans	0.50	1	0.50
Microscribe	1.00	2	2.00
Remove and measure muscle	1.00	2	2.00
Post-processing			
3D scan alignment and background removal	4.00	1	4.00

Appendix L. Visualization of all MRI 3D surface models

This figure was created to visualize the STL models generated from MRI segmentation of the individual muscles, grouped per dissection layer. In these dissection layers, the 3D scans were made, and the MRI 3D surface models of the bones and muscles were grouped into OBJs for co-registration.

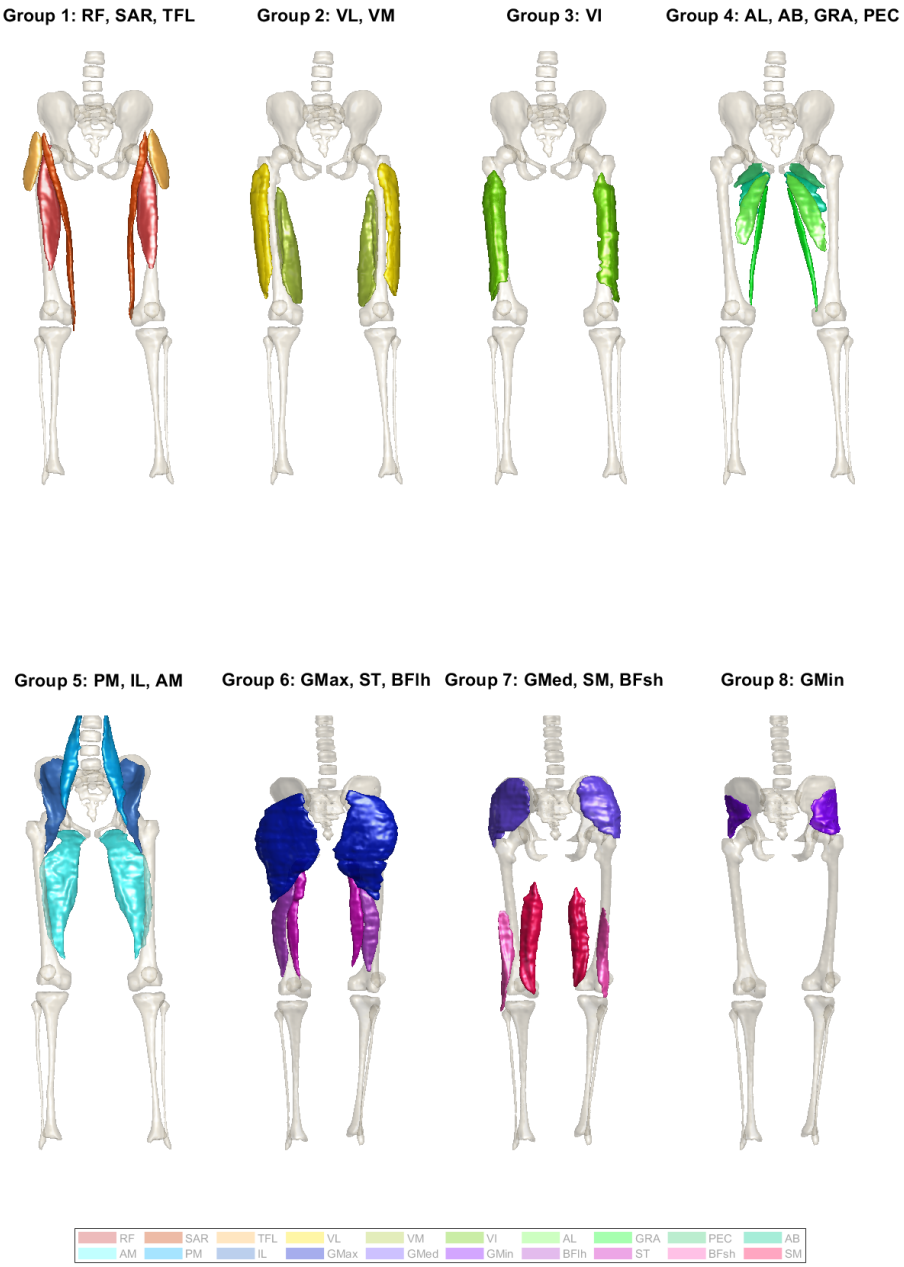

Figure L.25: MRI-derived 3D visualization of lower limb muscle groups. Eight anatomically-defined muscle groups are displayed for both legs, with supine groups (1-5) shown from an anterior view and prone groups (6-8) from a posterior view. Bone structures shown with transparency; muscles color-coded within each functional group.

Appendix M. Co-registered MRI-3D scan

All renders in this appendix were created using Blender in high-definition. The Blender API was set to use the Cycles rendering engine, a studio background, and an area light of 5×5 m. Renders were exported at a resolution of 2560×1440 pixels to ensure clarity and detail.

Appendix M.1. Prone group 1: GMax, ST, BFlh

Frontal view Side view Close up

Figure M.26: Co-registered 3D models of MRI 3D surface models and 3D scan of prone group 1: GMax (Blue), ST (Orange), BFlh (Yellow).

Appendix M.2. Prone group 2: GMed, SM, BFsh

Frontal view Side view Close up

Figure M.27: Co-registered 3D models of MRI 3D surface models and 3D scan of prone group 2: GMed (Blue), SM (Orange), BFsh (Yellow).

Appendix M.3. Prone group 3: GMin

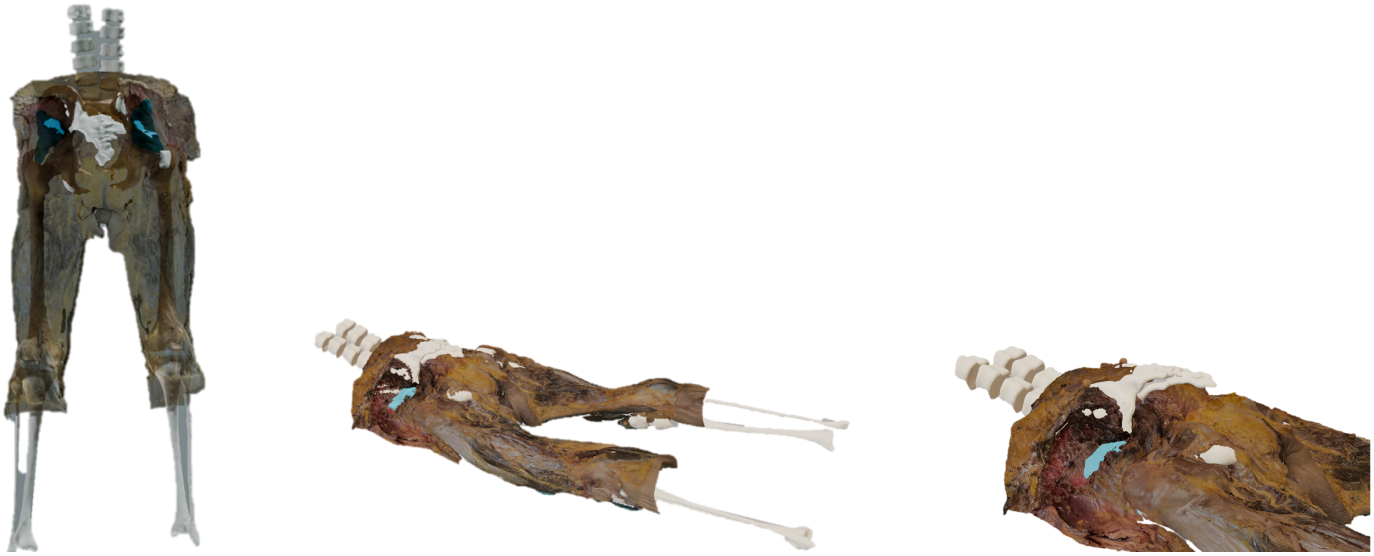

Frontal view Side view Close up

Figure M.28: Co-registered 3D models of MRI 3D surface models and 3D scan of prone group 3: GMin (Blue).

Appendix M.4. Supine group 1: RF, SAR, TFL

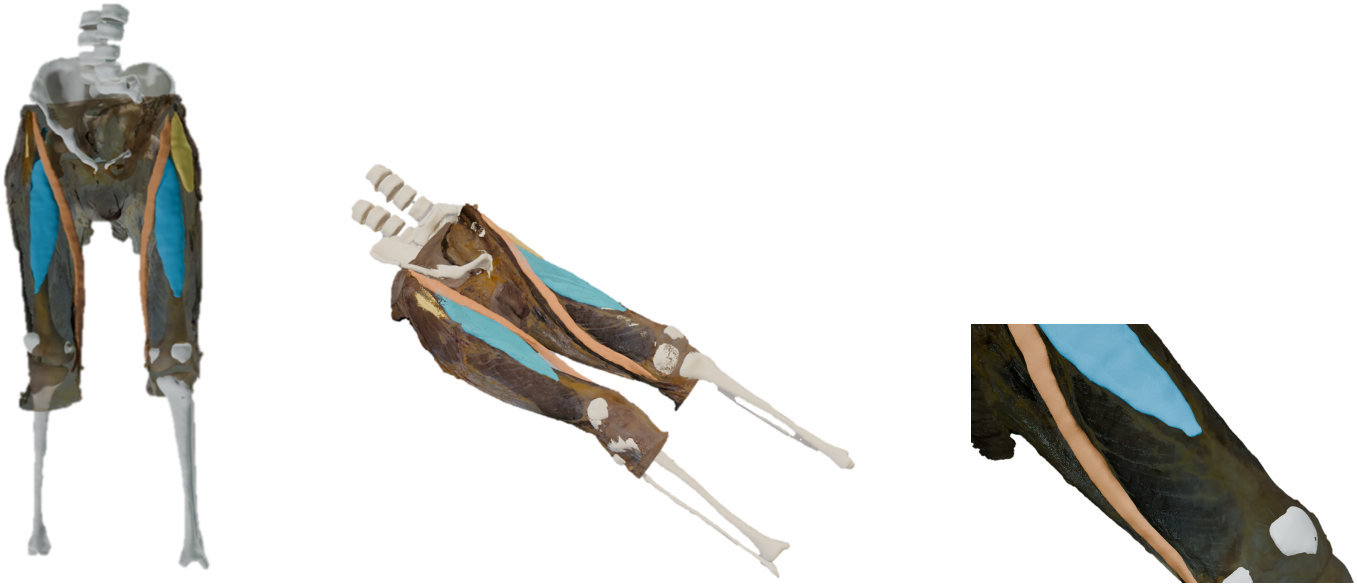

Frontal view Side view Close up

Figure M.29: Co-registered 3D models of MRI 3D surface models and 3D scan of supine group 1: RF (Blue), SAR (Orange), TFL (Yellow).

Appendix M.5. Supine group 2: VL, VM

Frontal view Side view Close up

Figure M.30: Co-registered 3D models of MRI 3D surface models and 3D scan of supine group 2: VL (Blue), VM (Orange).

Appendix M.6. Supine group 3: VI

Frontal view Side view Close up

Figure M.31: Co-registered 3D models of MRI 3D surface models and 3D scan of supine group 3: VI (Orange).

Appendix M.7. Supine group 4: AL, AB, GRA, PEC

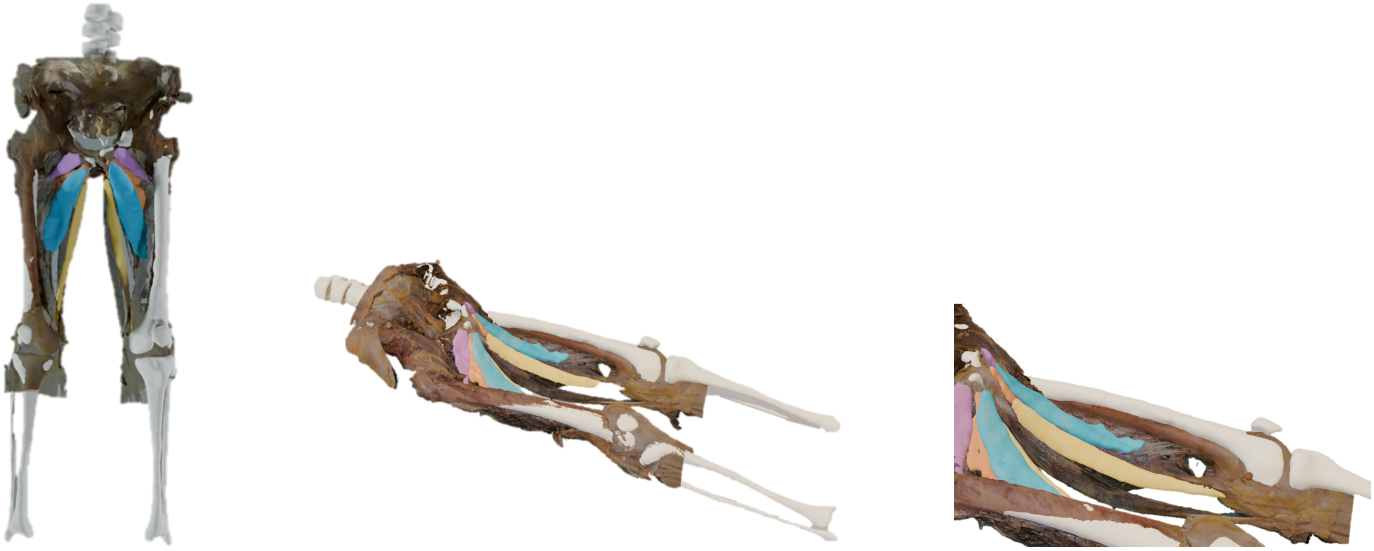

Frontal view Side view Close up

Figure M.32: Co-registered 3D models of MRI 3D surface models and 3D scan of supine group 4: AL (Blue), AB (Orange), GRA (Yellow), PEC (Purple).

Appendix M.8. Supine group 5: PM, IL, AM

Frontal view Side view Close up

Figure M.33: Co-registered 3D models of MRI 3D surface models and 3D scan of supine group 5: PM (Blue), IL (Orange), AM (Yellow).

Appendix N. Heatmap visualization muscle groups

All renders in this appendix were created using Blender. The Blender API was set to use the Cycles rendering engine, default background, and an area light of 5×5 m. Renders were exported at a resolution of 2560×1440 pixels to ensure clarity and detail.

(a) Supine group 1: RF, SAR, TFL

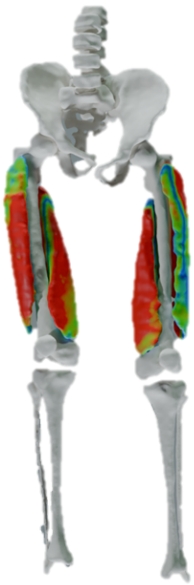

(b) Supine group 2: VL, VM

(c) Supine group 3: VI

(d) Supine group 4: AL, AB, GRA ,PEC

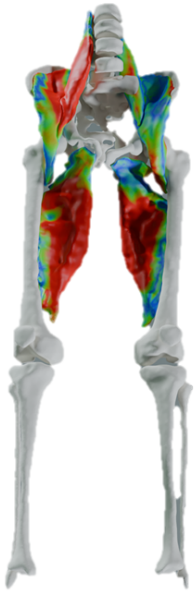

(e) Supine group 5: PM, IL, AM

(f) Prone group 1: GMax, ST, BFlh

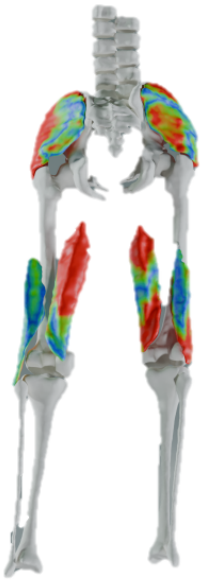

(g) Prone group 2: Gmed, SM, BFsh

(h) Prone group 3: Gmin

Figure N.34: Distance heatmaps show euclidean distances between aligned MRI-derived muscle models and 3D scan. **Blue regions** (0-2.5mm RMSE) indicate excellent alignment with minimal spatial deviation. **Green regions** (2.5-10mm RMSE) represent moderate alignment accuracy with acceptable registration errors. **Red regions** (> 10*mm* RMSE) highlight areas of poor alignment.

Appendix O. Fiber visibility

In this section an example of a 3D scan is shown to indicate the visibility and non-visibility of muscle fibers. In this example, a clear fiber structure can be seen in the gluteus maximus. However, no clear structure can be seen in the biceps femoris (long head) and the semitendinosus. This is due to the fact that the tendon plate of the biceps femoris inhibits good visibility of muscle fibers from the superficial surface.

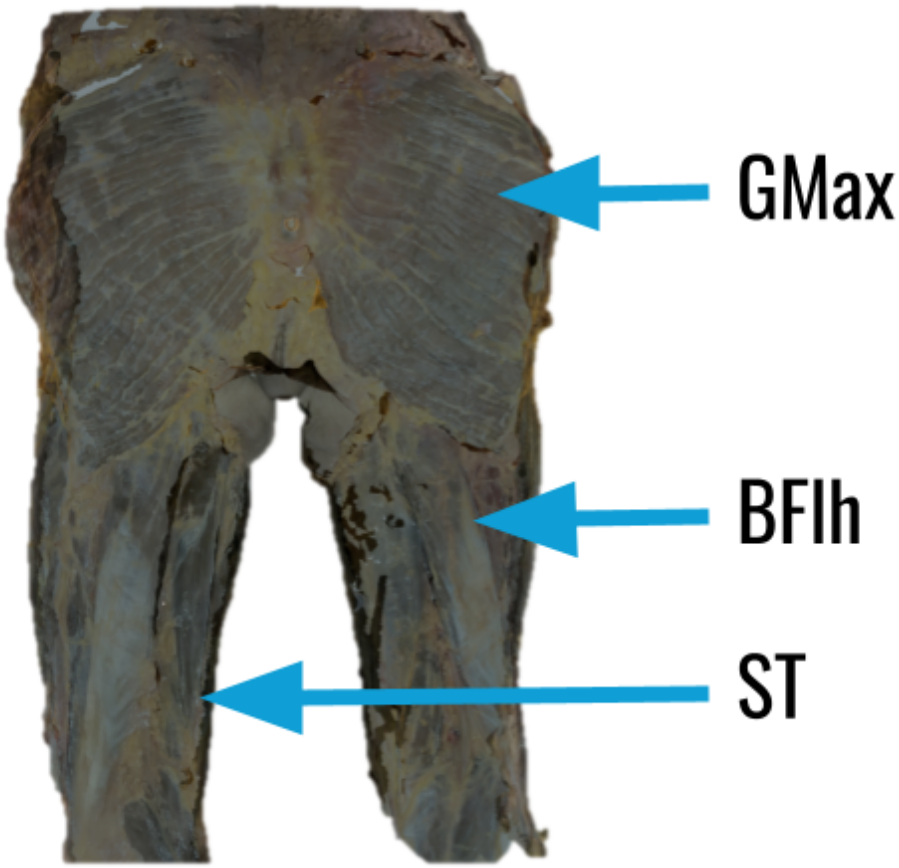

Figure O.35: Projected muscle fibers measured by the MicroScribe digitizer

Appendix P. Co-registered 3D scan and microscribe measured muscle fibers

This section is for the visualisation of measured muscle fibers on 3D scans and not for quantifying their accuracy. However, do note that these renders are subject to a cumulative alignment error of MRI-MS and MRI-3D scan. All renders in this appendix were created using Blender in high-definition. The Blender API was set to use the Cycles rendering engine, a studio background, and an area light of 5×5 m. Renders were exported at a resolution of 2560×1440 pixels to ensure clarity and detail.

Appendix P.1. Prone group 1: GMax, ST, BFlh

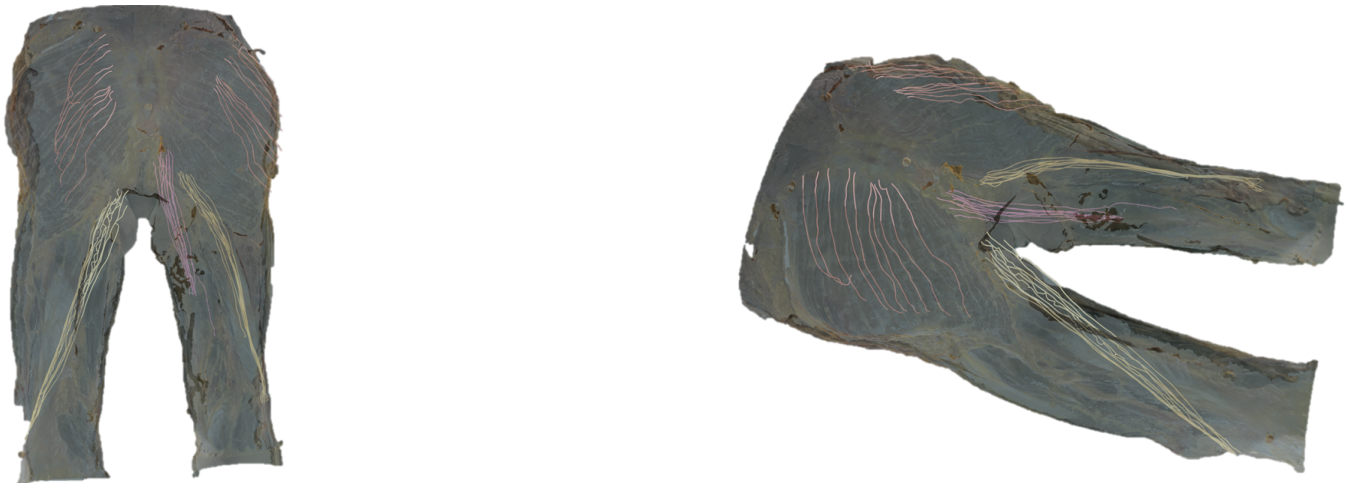

Frontal view Side view

Figure P.36: Co-registered 3D digitized of muscle fiber measurements and 3D scan of prone group 1: GMax (red), ST (pink), BFlh (yellow).

Appendix P.2. Prone group 2: GMed, SM, BFsh

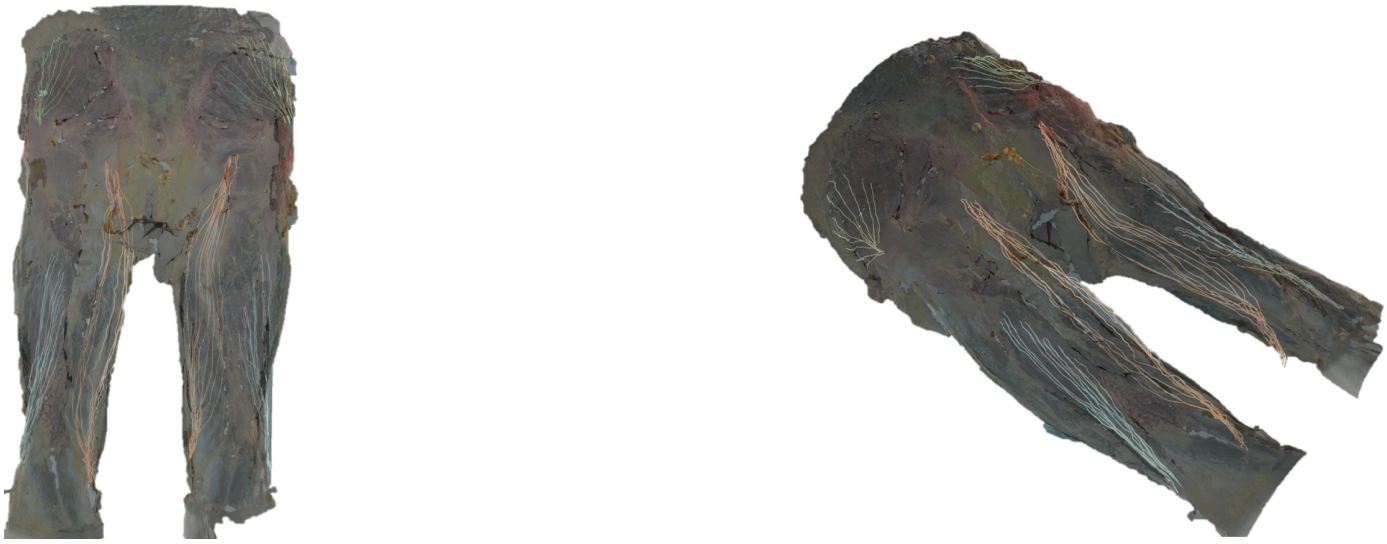

Frontal view Side view

Figure P.37: Co-registered 3D digitized of muscle fiber measurements and 3D scan of prone group 2: GMed (red), SM (orange), BFsh (blue).

Appendix P.3. Prone group 3: GMin

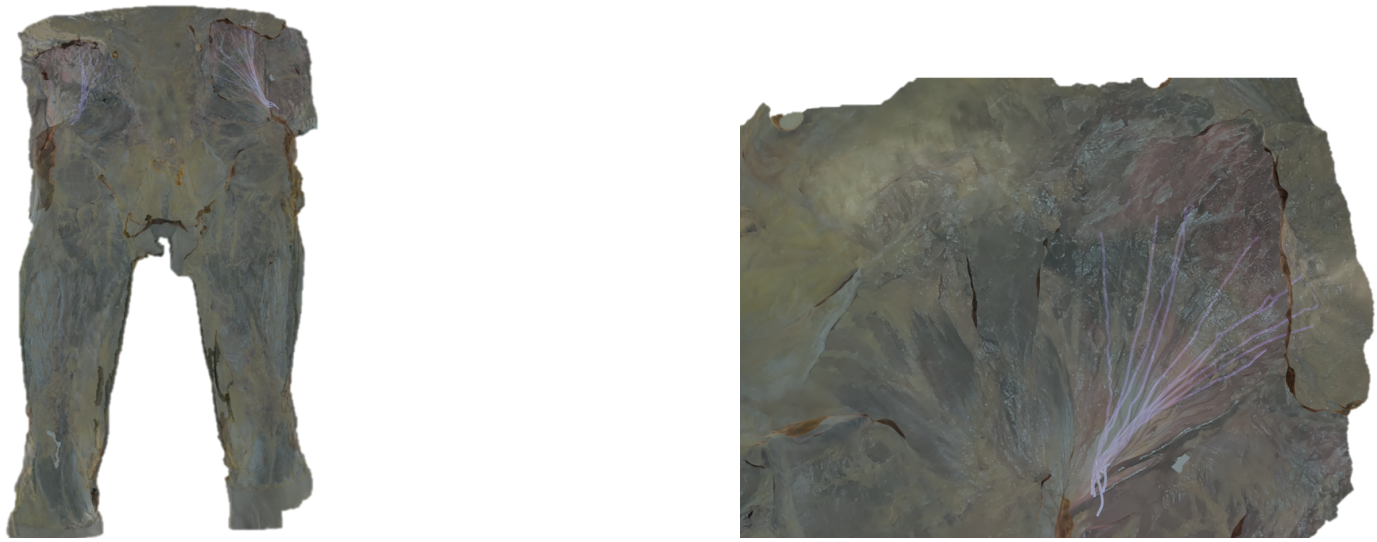

Frontal view Side view

Figure P.38: Co-registered 3D digitized of muscle fiber measurements and 3D scan of prone group 3: GMin (purple).

Appendix P.4. Supine group 1: RF, SAR, TFL

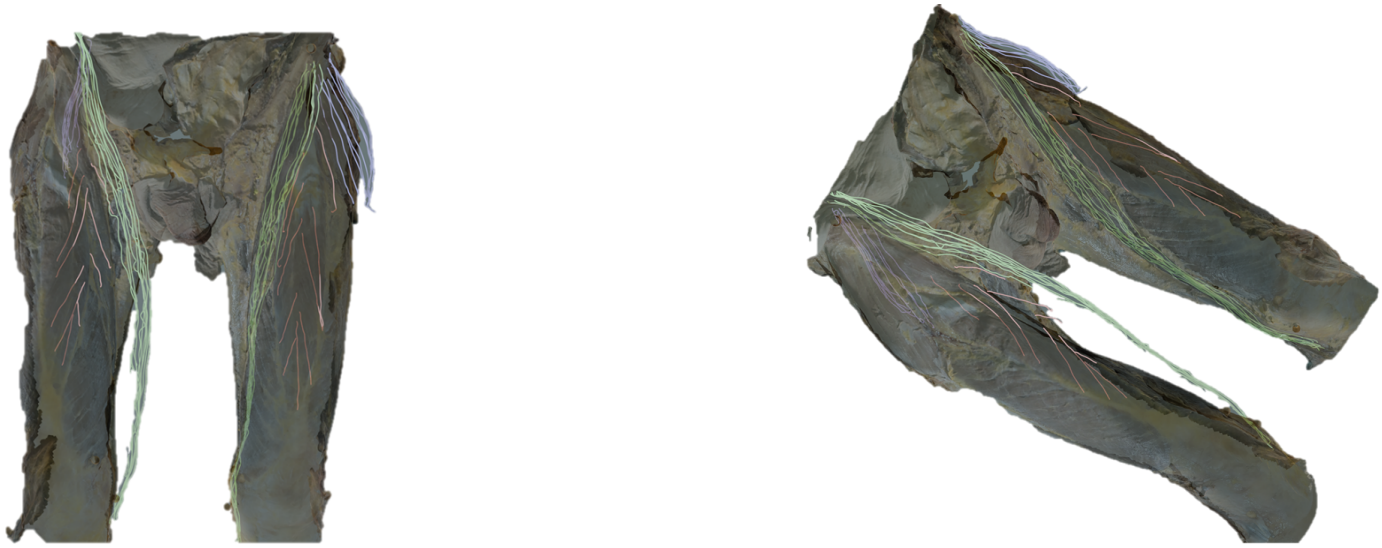

Frontal view Side view

Figure P.39: Co-registered 3D digitized of muscle fiber measurements and 3D scan of supine group 1: RF (red), SAR (green), TFL (blue).

Appendix P.5. Supine group 2: VL, VM

Frontal view Side view

Figure P.40: Co-registered 3D digitized of muscle fiber measurements and 3D scan of supine group 2: VL (orange), VM (pink).

Appendix P.6. Supine group 3: VI

Frontal view Side view

Figure P.41: Supine group 3: VI (blue).

Appendix P.7. Supine group 4: AL, AB, GRA, PEC

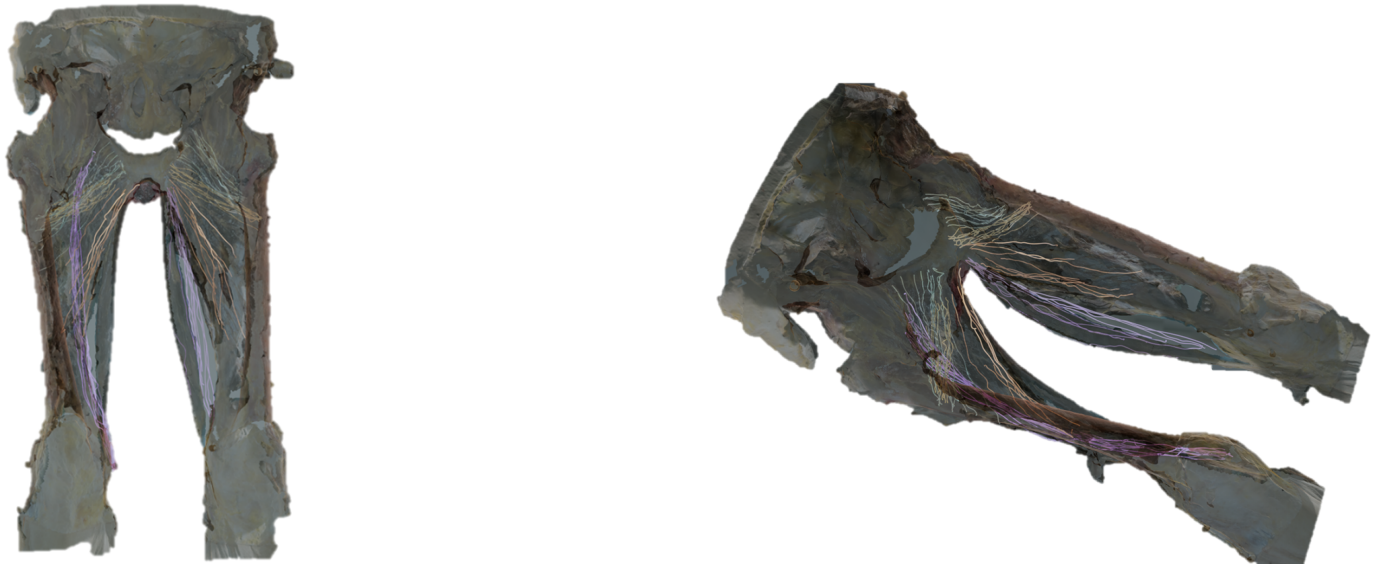

Frontal view Side view

Figure P.42: Co-registered 3D digitized of muscle fiber measurements and 3D scan of supine group 4: AL (orange), AB (Green), GRA (Purple), PEC (yellow).

Appendix P.8. Supine group 5: PM, IL, AM

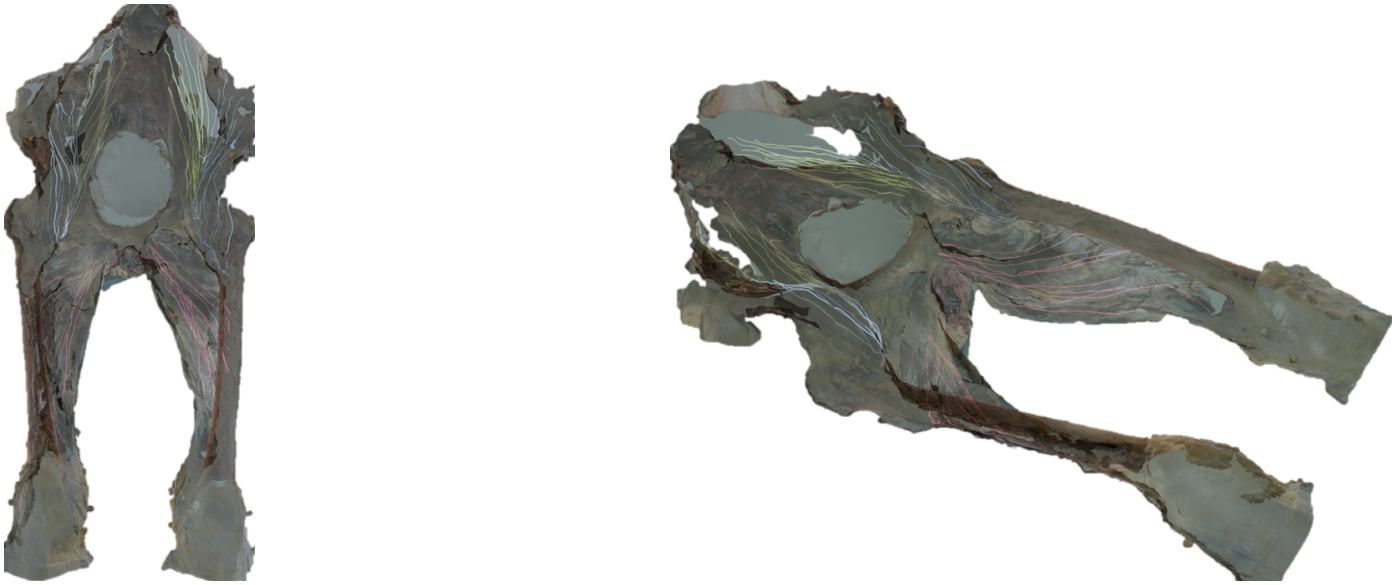

Frontal view Side view

Figure P.43: Co-registered 3D digitized of muscle fiber measurements and 3D scan of supine group 5: PM (yellow), IL (blue), AM (red).

Appendix Q. Annotation of muscle fiber length in 3D scans

Introduction

The aim of this study was to annotate muscle fibers on a 3D mesh derived from 3D scans using Blender software. The annotated fiber lengths were intended to be compared with muscle fiber lengths obtained from traditional 3D digitizer measurements. This approach was explored as a potential alternative method for non-invasive muscle fiber length assessment.

Materials and methods

Muscle fiber annotation was performed using the following procedure:

1. 3D scans were imported into Blender as high-resolution meshes
2. Vertices along the muscle fiber paths were manually selected
3. Lines were drawn through the selected vertices
4. Polylines were fitted through the points to represent muscle fiber trajectories
5. Fiber lengths were calculated from the fitted polylines

The left gluteus maximus muscle was used as the primary test case for this methodology.

Results

The implementation of this method revealed several significant challenges:

- The high resolution of the mesh required extensive annotation time due to the large number of vertices
- Visibility of muscle fiber locations was severely compromised as the photorealistic surface texture was obscured by the dense black vertices (Figure Q.44)
- The computational demands of the high-density mesh caused frequent Blender crashes, resulting in loss of selected vertices and annotation progress

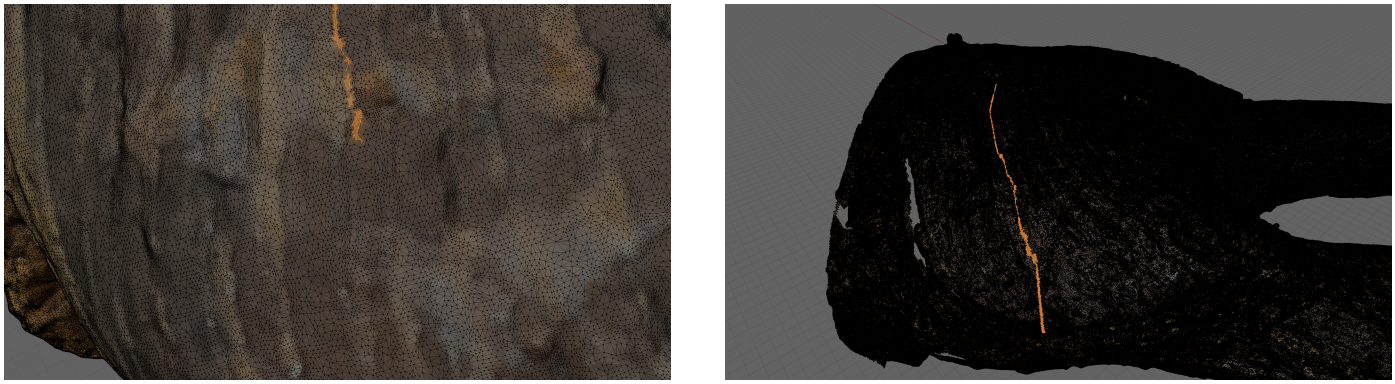

(a) Close-up view of selected vertices

(b) Zoomed-out view of selected vertices

Figure Q.44: Selected vertices on the left gluteus maximus muscle showing (a) the dense vertex distribution that obscures surface texture and (b) the extensive area requiring annotation

Discussion

The 3D mesh-based approach for muscle fiber length measurement proved to be significantly more time-consuming than traditional 3D digitizer measurements. While the method theoretically offers non-invasive assessment capabilities, several practical limitations emerged:

- The time investment required for accurate annotation exceeds that of direct digitizer measurements
- A potential alternative approach involving interpolation from fewer selected vertices might reduce time requirements but would likely compromise measurement accuracy
- The computational limitations of handling high-resolution meshes in Blender present a significant technical barrier
- The loss of visual surface information during vertex selection mode hinders accurate fiber path identification

Action points

Based on these findings, the following recommendations are made:

1. Due to time constraints and practical limitations, no further muscle fiber measurements were conducted using the 3D mesh method
2. The 3D scan approach is not recommended for routine muscle fiber length measurements given the excessive time requirements
3. For current applications, traditional 3D digitizer measurements remain the preferred method for muscle fiber length assessment

Appendix R. Muscle displacement and depth after fixation

Introduction

Fixation of biological tissues can induce structural changes that affect muscle architecture, but these changes are unlikely to be uniform across all muscles. Superficial muscles may undergo greater volume changes and deformation compared to deep muscles due to exposure to mechanical constraints from surrounding tissues. We hypothesized that superficial muscles would exhibit greater preservation-induced displacement than deep muscles during fixation.

Materials and methods

To test this hypothesis, 3D surface models of muscles were generated from MRI scans of both fresh (MRI_{fresh}) and fixated ($MRI_{fixated}$) cadaveric lower limbs. The Euclidean distance from each muscle centroid to the femur centroid was calculated from MRI_{fresh} models to quantify muscle depth.

Co-registration of the two MRI scan derived muscle 3D models

The 3D muscle reconstructions from both MRI scans (MRI_{fresh} and $MRI_{fixated}$) were aligned using Iterative Closest Point (ICP) registration of their respective femur models. The ICP algorithm iteratively minimized the distance between corresponding points on the femoral surfaces, with convergence criteria set to translation changes < 0.01 mm and rotation changes < 0.05 radians between consecutive iterations. A maximum of 100 iterations was allowed. The ICP registration was implemented through MATLAB's Computer Vision Toolbox functions. Following registration, the final root mean square error was calculated by finding the nearest neighbors between the aligned femur models, with values below 2 mm considered acceptable for alignment quality.

Analysis displacement

Muscle displacement due to fixation was measured as the Euclidean distance between the centroids of corresponding MRI_{fresh} and $MRI_{fixated}$ muscle models after alignment. Alignment of the femurs was performed using the Iterative Closest Point (ICP) algorithm, and the resulting transformation matrix was applied to register $MRI_{fixated}$ to MRI_{fresh}.

Correlation

The relationship between muscle depth and displacement was assessed using the Pearson correlation coefficient (r^2). Data from both left and right legs were pooled for analysis (n = 40 muscles).

Results

ICP iterations

The convergence curves demonstrate that both left and right femur bone registrations reached a stable plateau well before termination. The algorithm converged to RMS errors below the 2mm benchmark by iteration 10, with subsequent iterations showing minimal improvement. When the ICP algorithm terminated due to meeting the predefined convergence criteria (attenuation conditions), no additional iterations were necessary, as evidenced by the sustained plateau in error reduction. This confirms that the stopping conditions were effectively identified when further iterations would yield negligible improvements in registration accuracy.

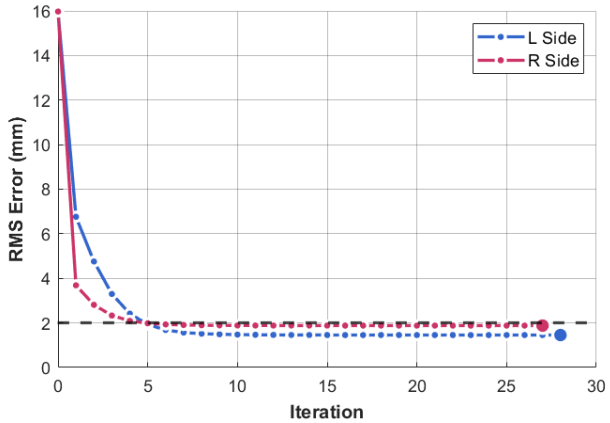

Figure R.45: ICP convergence analysis for MRI femur bone of $MRI_{fixated}$ matched with the 3D femur model of MRI_{fresh}. A black dashed line was added to indicate the 2 mm benchmark for the RMS error of the ICP.

Displacement

The mean displacement of muscle centroids between MRI_{fresh} and $MRI_{fixated}$ models was 12.1 ± 7.2 mm (range: 3.1 – 35.1 mm). The largest displacements were observed in the adductor muscles and psoas major, whereas the smallest displacements occurred in gluteus maximus and vastus intermedius. Correlation analysis indicated a negligible relationship between muscle depth and displacement (r^2 = 0.003), suggesting that fixation-induced displacement is essentially independent of the distance from the femur (table R.10 and figure R.46).

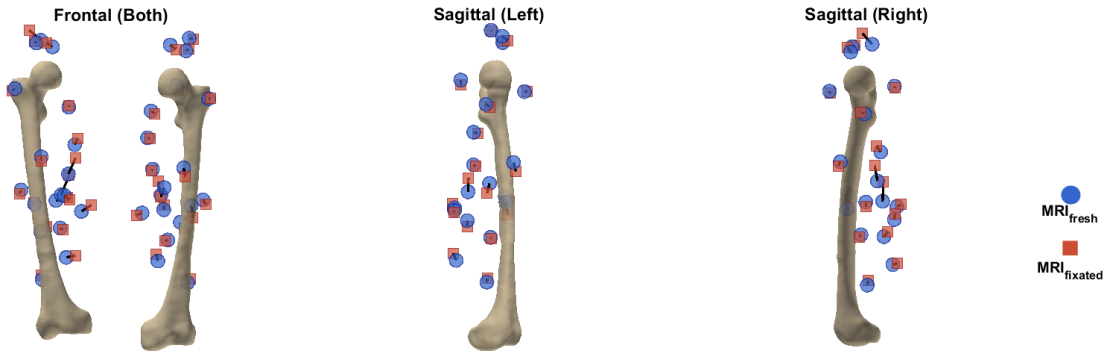

Figure R.46: Comparison of muscle centroid positions between MRI_{fresh} (blue) and $MRI_{fixated}$ (red) relative to the femur. Frontal view (left) shows both left and right femurs from the anterior perspective. Sagittal views (center and right) show left and right femurs individually from the medial side.

Table R.10: Muscle centroid displacement and depth measurements from spatial deformation analysis. Displacement represents the Euclidean distance between MRI_{fresh} and $MRI_{fixated}$ 3D surface model centroids after femur bone alignment. Depth represents the distance from each muscle's 3D surface model centroid to the femur 3D surface model centroid in MRI_{fresh}. L = left leg, R = right leg.

Muscle	Displacement (mm)		Depth (mm)	
	L	R	L	R
RF	14.6	7.4	83.4	85.4
SAR	16.4	11.5	54.0	36.2
TFL	4.7	6.3	196.9	198.8
VL	9.8	6.2	46.5	48.3
VM	6.6	7.6	42.8	41.0
VI	20.1	4.6	24.7	18.7
AL	5.7	30.9	90.5	68.1
GRA	10.1	20.8	75.8	71.3
PEC	7.8	7.1	177.3	165.8
AB	6.7	15.8	138.3	113.0
AM	22.6	35.1	59.8	48.7
PM	30.0	23.3	381.2	373.0
IL	12.4	11.8	278.2	259.5
GMax	8.4	3.1	219.8	211.9
GMed	7.0	26.2	288.0	270.2
GMin	5.8	7.2	267.4	265.1
BFlh	12.1	12.7	60.0	70.6
ST	7.9	18.8	71.8	70.0
BFsh	7.8	7.8	111.7	120.1
SM	12.2	15.0	99.4	102.7

Discussion

Although muscle volumes increased substantially, the relative positions of muscles to the skeleton did not show a systematic linear correlation with depth (r^2 = 0.003), suggesting that while fixation caused muscles to swell, it did not alter their positions within the leg. This finding contradicts the initial hypothesis that superficial muscles would exhibit greater displacement than deep muscles during the preservation process. Muscle centroid displacements ranged widely from 3.1 to 35.1 mm (mean: 12.7 ± 8.0mm), with the largest displacements observed in the adductor muscles and psoas major, while the smallest occurred in gluteus maximus and vastus intermedius. The muscles with the least displacement typically had larger insertion and origin attachment areas to bone compared to the longer, thinner muscles that showed greater displacement, likely also influenced by gravitational effects that caused them to hang downward during dissection.

Appendix S. Code flowchart

In the flowchart represented in S.47 the data flow of the analyses in this thesis can be seen. Matlab was necessary for the generation of 3D models and quantitative analysis, where Blender is a software that can be used to visualize 3D data well. Rhino is also a software that can be used to visualize data, but has an ancient python API and was thus not chosen for the further analysis of 3D data. Its integration with the Microscribe robot arm however was easy and interpretative, and therefore the software was used for the DIGI measurements.

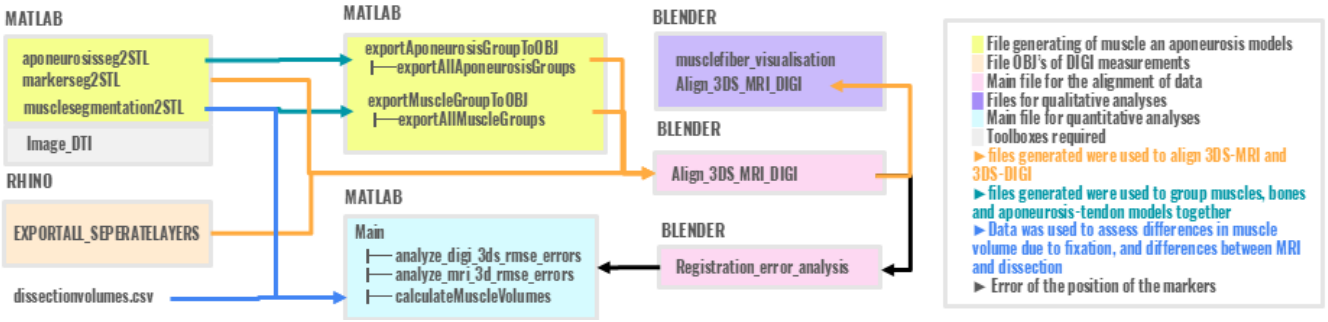

Figure S.47: In this flowchart the functions post-processing the data of MRI and DIGI can be seen. In addition the next alignments steps, and eventual analysis that were done (quantitative and qualitative) based on the generated data. The volumes and masses derived from dissection were not coded and manually measured, and are therefore inserted in this flowchart as a file.